

## FEATURE ARTICLE

## Ultrafast Nonlinear Spectroscopic Techniques in the Gas Phase and Their Density Matrix Representation

Bruna I. Grimberg, Vadim V. Lozovoy, and Marcos Dantus\*

*Department of Chemistry and Center for Fundamental Materials Research, Michigan State University, East Lansing, Michigan 48824*

Shaul Mukamel\*

*Department of Chemistry and Rochester Theory Center for Optical Science and Engineering, University of Rochester, P.O. RC Box 270216, Rochester, New York 14627**Received: February 6, 2001; In Final Form: October 23, 2001*

We survey the possible time-resolved three pulse nonlinear spectroscopic techniques and their application to gas-phase samples. The role of each of the interacting electric fields is specified, and the nature of the signal is interpreted using the density matrix representation. Simulations of these nonlinear optical signals are based on the perturbative solution of the Liouville equation for the density matrix to third order in the applied fields. We present closed expressions for the integrated and frequency dispersed signals that identify the type of molecular response for each technique and give the signal dependence on the various time delays between laser pulses. We choose a simple experimental system, two-electronic states coupled to a single vibrational mode of diatomic iodine, with weak dephasing, to illustrate various molecular polarization responses in four-wave mixing experiments including pump-probe, reverse transient grating, and photon echo. These signals and their simulations illustrate how the time delays between pulses can be effectively used to control the optical response of the molecular system.

## I. Introduction

The development of ultrafast tunable laser sources has allowed scientists in the past decade and a half to probe molecular dynamics with unprecedented femtosecond time resolution.<sup>1-6</sup> This tremendous progress in experimental capabilities has been accompanied in the theoretical front by a deeper understanding of the interaction between lasers and molecules using appropriate descriptions for these nonlinear optical processes. Two types of theoretical approaches have been employed in the interpretation of such experiments. Ultrafast measurements in the gas phase have been primarily analyzed

using a wave function representation and its evolution in Hilbert space,<sup>7-10</sup> whereas condensed phase measurements have commonly been analyzed using a density matrix formalism and its evolution in Liouville space.<sup>11-13</sup> The goal of this article is to discuss all possible signals that can be generated by ultrafast time-resolved experiments interacting resonantly with a molecular gas-phase system. The interpretation and simulation of the signals is based on the density matrix formalism and its diagrammatic representation, e.g., Feynman diagrams and ladder diagrams. The utility of the density matrix approach to femtosecond gas-phase measurements was first demonstrated<sup>14-16</sup> for the interpretation of gas-phase photodissociation pump-probe experiments<sup>17,18</sup> of ICN and later for the interpretation of three-pulse four-wave mixing in vapor I<sub>2</sub>.<sup>19</sup>

\* To whom correspondence should be addressed. dantus@msu.edu and mukamel@chem.rochester.edu

In this paper, we use a unified density matrix framework for understanding a broad range of ultrafast techniques used to interrogate molecular dynamics. In condensed phase spectroscopy, intermolecular contributions and dephasing processes are extremely important; these measurements are therefore often aimed at elucidating the response of the medium. In the case of liquid-phase experiments, this would be the response of the solvent and the subsequent relaxation dynamics. The macroscopic number of solvent molecules and the inherent inhomogeneity of the sample require a formulation that allows a *reduced description* based on a few relevant degrees of freedom, where the remaining ones are traced out.<sup>20–22</sup> Density matrix calculations naturally take into account the existence of all of the different species, their individual dynamics, different relaxation processes, and the coherent coupling between them caused by the laser fields.<sup>11–13,23</sup> Although a gas-phase sample is much more homogeneous, inhomogeneities caused by the initial distribution of rovibrational states and the distribution of velocities result in the static broadening (dephasing) of optical signals.<sup>24</sup> The density matrix formalism naturally incorporates the initial distribution of vibrational and rotational states from the outset, whereas in a wave function treatment the calculation needs to be repeated for each possible initial state and then averaged.

In addition to the observation of molecular dynamics, there has been a great interest in controlling chemical reactions with lasers. The basic principle behind these efforts is the use of a tailored electric field, which optimizes excitation of the molecular system to generate a preferred photochemical product.<sup>25,26</sup> These experiments have been carried out in the gas phase with pairs of phase-controlled pulses<sup>27,28</sup> or with a complex “shaped” laser pulse.<sup>29,30</sup> The density matrix approach underscores the coherent laser–molecule interactions, making clear the role of phase locking or phase matching among multiple pulses as well as the complex phase and amplitude modulation of shaped laser pulses. It is important to note that the diagrammatic representation of the density matrix can follow explicitly the time ordered coherent coupling that arises from successive interactions with multiple laser pulses; hence, it is particularly suitable for the simulation of coherent control. Maintaining time ordering in a wave function description is trickier. Several semiclassical wave-function-based calculations of experimental observables were based on forward–backward propagation in Hilbert space.<sup>31–33</sup> A semiclassical single trajectory calculation of the nonlinear response was developed by Yan and Mukamel.<sup>34</sup> A two trajectory algorithm for sampling the density matrix (for the bra and ket) was introduced by Sepulveda and Mukamel.<sup>35</sup> The semiclassical trajectory method using three-time correlation functions to describe resonance Raman spectra of iodine in the condensed phase was published by Ovchinnikov et al.<sup>36</sup> In contrast, in Liouville space, we only need to propagate forward trajectories. This makes the description much more intuitive and connected to multiple pulse experiments; we naturally follow the sequence of events as they occur in real time. For experiments in which the outcome depends on the electronic coherence induced by the pulses, the density matrix approach provides a straightforward tool to calculate the signal. Electronic coherence including all third order molecular responses are directly given by the off-diagonal elements of the density matrix. While using a wave function based formalism, we need to include all possible third-order contributions to the polarization  $P^{(3)} \propto \sum_i \langle \psi^{(i)} | \hat{\mu} | \psi^{(j)} \rangle$  with  $i + j = 3$ . Simulations of optical signals of medium size systems can be effectively performed using wave functions provided all

degrees of freedom are included explicitly.<sup>25,37–41</sup> Wave functions can no longer be used once a reduced description is adopted.

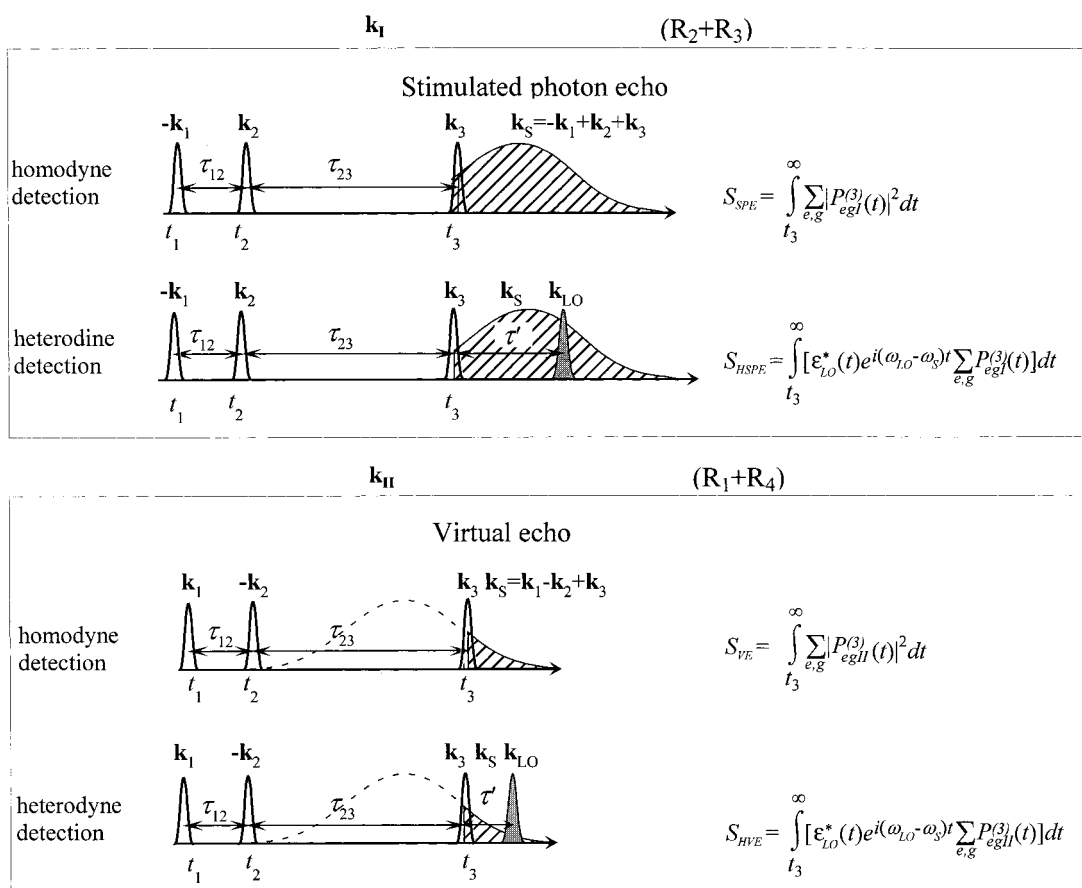
Gas-phase nonlinear FWM studies have a long history, starting probably with the observation of photon echoes in SF<sub>6</sub><sup>42</sup> and the first observation of molecular rotation by a third-order nonlinear process.<sup>43</sup> Numerous gas-phase applications of transient grating techniques were pioneered by Fayer, especially for the study of flames.<sup>44–46</sup> These novel probes have been applied to the study of femtosecond dynamics in the gas phase.<sup>19,47–61</sup> Zewail and co-workers used degenerate four-wave mixing (DFWM) for probing reaction dynamics.<sup>50</sup> Materny and co-workers have studied iodine vapor using time-resolved coherent anti-Stokes Raman scattering (CARS) and FWM.<sup>51–55</sup> By varying the time delay of one of the incident pulses while maintaining the other two incident pulses overlapped in time, they showed that vibrational and rotational dynamics can be observed for both the ground and excited electronic states. Prior and co-workers have used time-delay CARS to study high-energy ground-state vibrations.<sup>57,62</sup>

Brown et al.<sup>58</sup> used off-resonance transient grating methods to study the response of atoms as well as polyatomic molecules in the gas phase and derived a semiclassical expression to analyze the vibrational and rotational coherences observed in the data.<sup>63</sup> A number of reports have been published based on similar measurements in gas-phase samples.<sup>56,64–67</sup> Resonance transient grating measurements confirmed the observation of ground and excited states.<sup>58</sup> Dantus and co-workers have explored different laser pulse sequences in three-pulse FWM to control the observation of ground or excited-state dynamics.<sup>19,60,63</sup> They have shown that a spectrally dispersed three-pulse FWM method with transform limited and chirped pulses<sup>59,61</sup> adds an important dimension to the study of molecular events.

Experimental results obtained in a simple system, two electronic states of gas-phase molecular iodine, by a number of time-resolved four-wave mixing spectroscopies (pump–probe, reverse transient grating, and photon echo) are shown for illustration of the various molecular polarization responses. Gas-phase molecular iodine was chosen for various reasons. (i) The visible X <sup>1</sup>Σ<sub>0+g</sub> ↔ B <sup>3</sup>Π<sub>0+u</sub> transition has been well characterized by frequency<sup>68,69</sup> and time domain spectroscopies.<sup>19,51,59,61,70–72</sup> (ii) The vibrational periods of both the X and B states are longer than the duration of our laser pulses, allowing us to impulsively excite wave packets in each electronic state. (iii) The vibrational periods of the X and B states are very different, 160 and 307 fs, respectively, making the assignment of the signal relatively easy. (iv) At the wavelength of excitation, molecular iodine can be treated as a two (electronic) level system. The state reached by two-photon excitation is repulsive and does not contribute to the signals discussed in this article.

We use diagrammatic representations of the density matrix based on double-sided Feynman diagrams (DSFD) to depict the molecular response and its dependence on the pulse sequence.<sup>13</sup> The time delays between pulses are important experimental control parameters. The success of such experiments in directing the population and coherence transfer has been demonstrated recently.<sup>59–61,73</sup>

The theoretical foundations are presented in sections I–IV. Sections V–VIII contain experimental data and simulations. In section II, we apply the density matrix approach to calculate the induced polarization and the signal of multiple pulse spectroscopic techniques. The double-sided Feynman diagram and ladder diagram representations of the time-dependent density

TABLE 1: Characteristics of the  $S_I$  and  $S_{II}$  Three-Pulse FWM Signals for Nonoverlapping Pulses<sup>a</sup>

<sup>a</sup> Shown are the detection direction  $\mathbf{k}_S$ , the molecular responses that contribute to the signals, the pulse sequence, and an expression for the homodyne and heterodyne signals in terms of the third-order polarization, for detection.  $\tau_{ij}$  ( $i, j = 1, 2$ , and  $3$ ) is the time delay between the pulses.  $\tau'$  is the delay time of the local oscillator field for the heterodyned. In the detection direction  $\mathbf{k}_I$  ( $\mathbf{k}_{II}$ ), the signal is known as stimulated photon echo (virtual echo).

matrix and expressions for the resonant three-pulse FWM signal for different nonlinear processes are given and summarized in Figure 2. In section III, we present general expressions for FWM signals in a multilevel system. Expressions are also given for two-dimensional FWM signals, displayed as a function of two experimental variables: the central frequency of the detector and the time delay of the scanning pulse. In section IV, we apply these results to a four-level system, representing two electronic states each containing two vibrational levels. Using this model, we illustrate how different pulse sequences can be used to select individual molecular responses (i.e., *Liouville space pathways*). In section V, we present experimental results illustrating different FWM signals obtained with three well-separated pulses. The pulse sequences, the molecular responses that contribute to the signal, and the expressions of the signals in terms of the third order polarization are summarized in Table 1. Two-dimensional experimental data and their simulations based on the density matrix approach are also included. In section VI, we present experimental data for different nonlinear FWM signals obtained when one pair of pulses temporally overlap. The pulse sequences, the molecular responses that contribute to the signal, and expressions for the signals in terms of the third-order polarization are given in Table 2. In section VII, we discuss cascaded FWM signals. An expression for the signal based on the density matrix formulation and experimental results along with their simulation are presented. Pump-probe techniques are discussed in section VIII. The pulse sequences, molecular responses that contribute to the signal and expressions

for the signal in terms of the third-order polarization are given in Table 3. Section IX concludes this article with a review of the most popular ultrafast nonlinear spectroscopic techniques and a summary of the merits of the density matrix formulation for understanding and simulating gas phase multiple-pulse nonlinear spectroscopies.

## II. Density Matrix Calculation of Nonlinear Response Functions

The density matrix provides a statistical description of quantum systems.<sup>74,75</sup> Formally, the density matrix is defined using the outer product of the state of the system  $|\text{ket}\rangle$  with its Hermitian conjugate  $\langle\text{bra}|$

$$\hat{\rho}(t) = \sum_j P_j |\Psi_j(t)\rangle \langle\Psi_j(t)| \quad (1)$$

Equation 1 describes a statistical ensemble (a mixed state) where the system has a probability  $P_j$  to be in the state  $|\Psi_j\rangle$  with  $\sum_j P_j = 1$ . When  $P_j = 1$  for one state and is zero, otherwise, the system is in a *pure state* (a state with maximum information) and can be described by a wave function. Otherwise, we have a *mixed state* that may not be described by a single wave function. Adopting a basis set ( $\varphi_a$ ), we have

$$|\Psi_j(t)\rangle = \sum_a \alpha_{ja}(t) |\varphi_a\rangle \quad (2)$$

**TABLE 2: Characteristics of Three-Pulse FWM Signals Where Two Pulses Overlap in Time<sup>a</sup>**

		$\mathbf{k}_I$	$(R_2+R_3)$	
<b>Photon echo</b>				
homodyne detection				$S_{PE} = \int_{t_2}^{\infty} \sum_{e,g}  P_{eg}^{(3)}(t) ^2 dt$
heterodyne detection				$S_{HPE} = \int_{t_2}^{\infty} [\mathcal{E}_{LO}^*(t) e^{i(\omega_{LO} - \omega_s)t} \sum_{e,g} P_{eg}^{(3)}(t)] dt$
<b>Reverse transient grating</b>				
$\mathbf{k}_{II} \quad (R_1+R_4)$				
homodyne detection				$S_{RTG} = \int_{t_2}^{\infty} \sum_{e,g}  P_{egII}^{(3)}(t) ^2 dt$
heterodyne detection				$S_{HRTG} = \int_{t_2}^{\infty} [\mathcal{E}_{LO}^*(t) e^{i(\omega_{LO} - \omega_s)t} \sum_{e,g} P_{egII}^{(3)}(t)] dt$
<b>Transient grating</b>				
$\mathbf{k}_I + \mathbf{k}_{II} \quad (R_2+R_3+R_1+R_4)$				
homodyne detection				$S_{TG} = \int_{t_2}^{\infty} \sum_{e,g}  P_{egII}^{(3)}(t) ^2 dt$
heterodyne detection				$S_{HTG} = \int_{t_2}^{\infty} [\mathcal{E}_{LO}^*(t) e^{i(\omega_{LO} - \omega_s)t} \sum_{e,g} P_{egII}^{(3)}(t)] dt$

<sup>a</sup> Only sequences that survive the RWA for a two electronic level model are shown. Shown are the detection direction  $\mathbf{k}_S$ , the molecular responses that contribute to the signal, the pulse sequence, and an expression for the signals in terms of the third-order polarization, for homodyne and heterodyne detection. The delay time between the pulses,  $\tau_{ij}$  ( $i, j = 1, 2$ , and  $3$ ), is shown in the pulse sequences. The delay time of the local oscillator field,  $\tau'$ , for the heterodyne measurements is indicated as well. In the detection direction  $\mathbf{k}_I$ , we obtain photon echo measurements, whereas for detection direction  $\mathbf{k}_{II}$ , we observe reverse transient grating process. Transient grating measurements can be obtained in both detection directions.

and the elements of the density matrix are given by

$$\rho_{ab}(t) = \sum_j P_j \langle \varphi_a | \Psi_j(t) \rangle \langle \Psi_j(t) | \varphi_b \rangle = \sum_j P_j \alpha_{ja} \alpha_{jb}^* \quad (3)$$

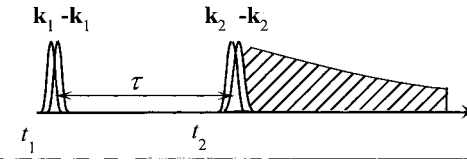
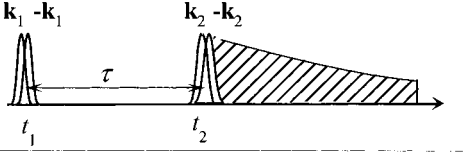
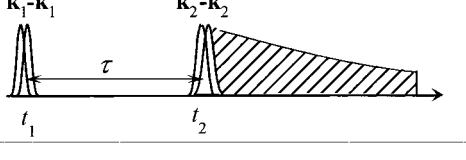
The diagonal element,  $\rho_{aa}$ , represents the probability that the system is in the state  $|\varphi_a\rangle$ , i.e., the *population* of that state. The off-diagonal elements,  $\rho_{ab}$ , represent the phase relationship between  $|\varphi_a\rangle$  and  $|\varphi_b\rangle$  and are denoted as the *coherence* between these states.

The time evolution of the density matrix,  $\hat{\rho}(t)$ , can be calculated by solving the Liouville equation:

$$\frac{\partial \hat{\rho}(t)}{\partial t} = -\frac{i}{\hbar} [\hat{H}(\mathbf{r}), \hat{\rho}(t)] - \hat{\gamma} \hat{\rho}(t) \quad (4)$$

where the square brackets represents the commutator. The Hamiltonian operator  $\hat{H}(\mathbf{r})$  can be separated as  $\hat{H}(\mathbf{r}) = \hat{H}_0(\mathbf{r}) + \hat{V}(\mathbf{r}, t)$ , where  $\hat{H}_0(\mathbf{r})$  is the unperturbed Hamiltonian and  $\hat{V}(\mathbf{r}, t) = -\hat{\mu} \cdot \mathbf{E}(\mathbf{r}, t)$  is the interaction with the external electric field

TABLE 3: Characteristics of Coherent Pump–Probe Signals<sup>a</sup>

coherent pump-probe (heterodyne detected transient grating)		
(R <sub>1</sub> +R <sub>2</sub> +R <sub>3</sub> +R <sub>4</sub> )		
degenerate		$S_{pp} = \int_{-\infty}^{\infty} [\mathcal{E}_2^*(t) e^{i(\omega_{LO} - \omega_3)t} \sum_{e,g} (P_{egI}^{(3)} + P_{egII}^{(3)}(t))] dt$
(R <sub>1</sub> +R <sub>2</sub> )		
excited state		$S_{pp} = \int_{-\infty}^{\infty} [\mathcal{E}_2^*(t) e^{i(\omega_{LO} - \omega_3)t} \sum_{e,g} (P_{egI}^{(3)} + P_{egII}^{(3)}(t))] dt$
(R <sub>3</sub> +R <sub>4</sub> )		
ground state		$S_{pp} = \int_{-\infty}^{\infty} [\mathcal{E}_2^*(t) e^{i(\omega_{LO} - \omega_3)t} \sum_{e,g} (P_{egI}^{(3)} + P_{egII}^{(3)}(t))] dt$

<sup>a</sup> Only sequences that survive the RWA for a two electronic level model are shown. The Table includes the molecular responses that contribute to the signal, the pulse sequences, and the expression for the signals in terms of the third-order polarization and the local oscillator field,  $E_2^*(\tau', t)$ , for heterodyne detection. The scanning time,  $\tau$ , is shown in the pulse sequences.

( $\mathbf{r}$  is the spatial coordinate of the sample), and  $\hat{\mu}$  the coupling operator.  $\hat{\gamma}$  is the relaxation superoperator.<sup>76–78</sup>

The perturbative solution of the Liouville equation is obtained by expanding the density matrix, in powers of the incoming field.<sup>12,13,79</sup>

$$\rho_{ab}(t) = \rho_{ab}^{(0)}(t) + \rho_{ab}^{(1)}(t) + \rho_{ab}^{(2)}(t) + \dots \quad (5)$$

where the  $n$ th term  $\rho_{ab}^{(n)}(t)$  represents the change of the density matrix element after an  $n$ th order interaction with the external electric field. Substituting eq 5 in eq 4 and collecting terms to  $n$ th order in the field gives

$$\frac{d\rho_{ab}^{(n)}(\mathbf{r}, t)}{dt} = (-i\omega_{ab} - \gamma_{ab})\rho_{ab}^{(n)}(\mathbf{r}, t) + \frac{iE(\mathbf{r}, t)}{\hbar} \sum_c \mu_{ac} \rho_{cb}^{(n-1)}(\mathbf{r}, t) - \rho_{ac}^{(n-1)}(\mathbf{r}, t) \mu_{cb} \quad (6)$$

In eq 6 and hereafter, we assume  $\hat{\gamma}$  to be diagonal. Each density matrix element has a relaxation rate  $\gamma_{ab} = 1/2(\Gamma_a + \Gamma_b) + \hat{\Gamma}_{ab}$  representing the sum of the inverse of the lifetimes ( $\Gamma_a + \Gamma_b$ ) of the levels involved in the transition and the pure dephasing rate ( $\hat{\Gamma}_{ab}$ ) because of intermolecular collisions. The transition frequency is  $\omega_{ab} = (\bar{E}_a - \bar{E}_b)/\hbar$  where  $\bar{E}_j$  is the energy of level  $j$ . The external electric field consists of successive well-separated pulses (i.e., pulses shorter than their delay periods):

$$E(\mathbf{r}, t) = \sum_n E_n(\mathbf{r}, t - t_n) \quad (7)$$

The solution of the Liouville equation is then given by

$$\rho_{ab}^{(n)}(\mathbf{r}, t) = \frac{i}{\hbar} I_{ab}(t - t_n) \int_{-\infty}^t dt' E_n(\mathbf{r}, t' - t_n) \exp[i(\omega_{ab} + \gamma_{ab})(t' - t_n)] \sum_c \{ \mu_{ac} \rho_{cb}^{(n-1)}(\mathbf{r}, t') - \rho_{ac}^{(n-1)}(\mathbf{r}, t') \mu_{cb} \} \quad (8)$$

where

$$I_{ab}(t - t_n) \equiv \exp[-(i\omega_{ab} + \gamma_{ab})(t - t_n)] \quad (9)$$

Because the field is weak and short, we can safely assume a perturbative expansion whereby each pulse produces a first-order interaction. In the impulsive limit, when the relevant molecular time scales, including the relaxation times, are longer than the pulse duration, the upper limit of the integral in eq 8 can be set to infinity,  $t \rightarrow \infty$ . We then obtain the following expression for the time dependent density matrix:

$$\rho_{ab}^{(n)}(\mathbf{r}, t) = \frac{i}{\hbar} I_{ab}(t - t_n) \sum_c [V_{ac,n} \rho_{cb}^{(n-1)}(\mathbf{r}, t_n) - \rho_{ac}^{(n-1)}(\mathbf{r}, t_n) V_{cb,n}] \quad (10)$$

with the effective coupling

$$V_{ac,n} \equiv \mu_{ac} \int_{-\infty}^{\infty} dt E_n(\mathbf{r}, t - t_n) \exp[i\omega_{ac} t] \quad (11)$$

To highlight the role of the phase and spatial profile, it is convenient to expand each pulse in the following way:

$$E_n(\mathbf{r}, t - t_n) = \epsilon_n(t - t_n) \exp[-i(\omega_n t - \mathbf{k}_n \cdot \mathbf{r})] + \epsilon_n^*(t - t_n) \exp[i(\omega_n t - \mathbf{k}_n \cdot \mathbf{r})] \quad (12)$$

where  $\epsilon_n(t - t_n)$  is the complex envelope of the  $n$ th pulse,  $\omega_n(\omega_n > 0)$  is the carrier frequency, and  $\mathbf{k}_n$  is the wave vector. The effective coupling matrix element can now be expressed as

$$V_{ac,n} = \mu_{ac}[\tilde{\epsilon}_n(\omega_{ac} - \omega_n) \exp[i\mathbf{k}_n \cdot \mathbf{r}] + \tilde{\epsilon}_n^*(\omega_{ac} + \omega_n) \exp[-i\mathbf{k}_n \cdot \mathbf{r}]] \equiv V_{ac,n}^+ + V_{ac,n}^- \quad (13)$$

where  $\tilde{\epsilon}_n(\omega) \equiv \int \epsilon_n(t) \exp(i\omega t) dt$  is the spectral envelope of the  $n$ th pulse. This amplitude peaks around  $\tilde{\epsilon}_n(0)$  and is negligible at optical frequencies because the carrier frequency  $\omega_{ac}$  has been removed. Note that, only in one of the two terms of eq 13, the optical frequency is canceled by the transition frequency  $\omega_{ac}$  depending on whether it is positive (excitation of a ket or deexcitation of a bra) or negative (deexcitation of a ket or excitation of a bra). We shall only retain this resonant term in the calculation of the signal; this is known as the rotating wave approximation (RWA). Each term of the interaction operator has a well-defined direction ( $\mathbf{k}_n$  or  $-\mathbf{k}_n$ ). Therefore, because of the selectivity imposed by the RWA, each pulse interaction contributes in a unique way to the phase matching direction of the nonlinear signal.

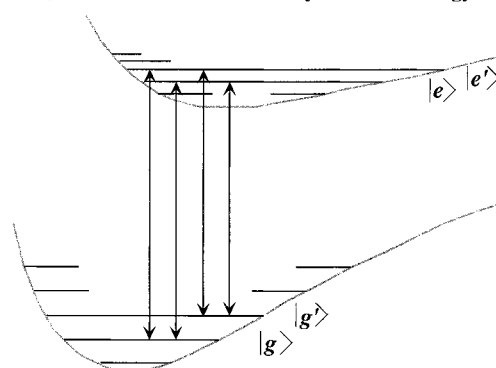
From eq 10, we see that the  $n$ th order density matrix element is obtained from the interaction between the applied field and  $\hat{\rho}^{(n-1)}(\mathbf{r}, t_n)$ . Equation 10 can be expressed in an operator form

$$\rho_{ab}^{(n)}(\mathbf{r}, t) = \frac{i}{\hbar} \int_{t_n}^t \hat{V}_n \hat{\rho}^{(n-1)}(\mathbf{r}, t_n) dt \quad (14)$$

where  $\hat{V}_n$  is the interaction operator with the  $n$ th pulse, whose matrix elements are given by the eq 13. According to eq 14, the interactions take place at the nodes,  $[\hat{V}_n, \hat{\rho}^{(n-1)}(\mathbf{r}, t_n)]$ , when a pulse is applied at time  $t_n$ . Each field selectively acts either on the bra or on the ket, incrementing by 1 the order of interaction. After the interaction, the density matrix propagates field-free with the propagator  $I(t)$  until the next pulse is applied. If eq 10 is expressed as a function of  $\hat{\rho}^{(0)}$ , the time evolution of the matrix elements  $\rho_{ab}^{(n)}(\mathbf{r}, t_n)$  is given by the sum of all possible pulse sequences that interact with the sample. Each term in this sum can be associated with a Liouville-space pathway,<sup>13</sup> and  $\rho_{ab}^{(n)}(\mathbf{r}, t)$  is given by the sum of all of these pathways. Closed expressions for  $\hat{\rho}^{(1)}(\mathbf{r}, t)$ ,  $\hat{\rho}^{(2)}(\mathbf{r}, t)$ , and  $\hat{\rho}^{(3)}(\mathbf{r}, t)$  for a general multilevel system are given in Appendix A.

From now on, we will focus on a two electronic level system with a ground-state vibrational manifold, ( $g, g', \dots$ ) and an excited-state vibrational manifold ( $e, e', \dots$ ) coupled by an electronic transition dipole operator. This system is illustrated in Figure 1a, which shows two potential energy curves along with the electronic dipole interactions,  $-\mu_{eg}E$ . The transitions between bound states take place in the Franck–Condon region of the potential energy curves and are represented by vertical arrows. A density matrix representation of this system and the changes under successive interactions with the electric field are presented in Figure 1b. Each change corresponds to a different order of interaction with the electric field. The initial density matrix,  $\hat{\rho}^{(0)}$ , contains only ground-state populations, indicated by the diagonal elements such as  $\rho_{gg}^{(0)}$  and  $\rho_{g'g'}^{(0)}$ . The first electric field interaction leads to an electronic coherence. Only the off-diagonal matrix elements representing the couplings between different electronic states are nonzero, such as  $\rho_{e'g}^{(1)}$  and its complex conjugate  $\rho_{g'e'}^{(1)}$ . The second-order density matrix, obtained after two interactions with the electric field, contains ground (such as  $\rho_{gg}^{(2)}$ ) and excited state (such as  $\rho_{e'e}^{(2)}$ ) popula-

a) One-Dimensional Model System and Energy Levels



b) Corresponding Multilevel Density Matrix

$\rho^{(0)}$		$\rho^{(1)}$		$\rho^{(2)}$	
$\rho_{gg}$	0	0	0	$\rho_{gg}$	$\rho_{gg}$
0	$\rho_{g'g'}$	0	0	$\rho_{g'e}$	$\rho_{g'e}$
0	0	0	0	$\rho_{g'e'}$	$\rho_{g'e'}$
0	0	$\rho_{e'g}$	$\rho_{e'g}$	0	0
0	0	$\rho_{g'e}$	$\rho_{g'e}$	0	0
0	0	$\rho_{e'g'}$	$\rho_{e'g'}$	0	0
0	0	$\rho_{g'e'}$	$\rho_{g'e'}$	$\rho_{ee}$	$\rho_{ee}$
0	0	0	0	$\rho_{e'e}$	$\rho_{e'e}$

**Figure 1.** (a) Energy diagram showing two potential energy surfaces with dipole interactions  $-\mu \cdot \mathbf{E}(\mathbf{r}, t)$ , (double vertical arrows) of their vibrational levels. For simplicity, only two vibrational levels in each electronic state are shown. (b) Representation of a multilevel density matrix before electric field interaction  $\hat{\rho}^{(0)}$  and after one  $\hat{\rho}^{(1)}$  and two electric field interactions  $\hat{\rho}^{(2)}$ . The initial density matrix contains only the population of the vibrational levels,  $\rho_{gg}^{(0)}$  and  $\rho_{g'g'}^{(0)}$ . The darkest diagonal terms correspond to the populations, and the gray off diagonal terms correspond to the vibrational coherence within each electronic state. The off diagonal elements in  $\hat{\rho}^{(1)}$  correspond to vibronic coherences, whereas those in  $\hat{\rho}^{(2)}$  correspond to vibrational coherences.

tions and vibrational coherence within each electronic state, such as  $\rho_{g'g'}^{(2)}$  and  $\rho_{e'e}^{(2)}$ .

The time evolution of the density matrix of the optically driven molecule can be represented diagrammatically by either the Liouville space coupling representation, the DSFD,<sup>13</sup> or the ladder diagrams.<sup>80</sup> Each diagram represents a distinct Liouville-space pathway. In Figure 2, we show the diagrammatic representation corresponding to the lowest three orders of the resonant dipole interaction applied to a system with two electronic states. In the Liouville space coupling representation, (left column) the state of the system is designated by a point in Liouville space, with indices corresponding to the ket–bra “axis”. Transitions on the ket are indicated with a vertical line between the points, whereas horizontal lines represent transitions on the bra. The DSFD shown in the second column can be described as follows: the vertical left and right lines of the diagram represent the time evolution (bottom to top) of the ket and bra, respectively; the applied electric fields are indicated with arrows oriented toward the left if propagating with a negative wave vector and vice versa for a positive wave vector. Each interaction with the electric field produces a transition between the two electronic states of either the bra or the ket. The ladder diagrams are shown in the third column. In this representation, the solid and dashed lines correspond to ket and bra interactions, respectively. Time evolves from left to right. The ability to track the evolution of the bra and ket simultaneously makes the density matrix a most appropriate tool for the description of many dynamical phenomena in nonlinear optical processes.

Response function	Liouville pathway	Feynman diagram	Ladder diagram	Formula
a) $P^{(1)}$				
J				$\rho_{eg}^{(1)}(t) = -iI_{eg}(t-t_1)V_{eg,1}^+\rho_{gg}^{(0)}$
J*				$\rho_{ge}^{(1)}(t) = -iI_{eg}^*(t-t_1)V_{eg,1}^-\rho_{gg}^{(0)}$
b) $P^{(2)}$				
Q <sub>1</sub>				$\rho_{gg}^{(2)}(t) = i^2I_{gg}(t-t_2)\sum_e V_{eg,2}^- I_{eg}(\tau_{12}) V_{eg,1}^+ \rho_{gg}^{(0)}$
Q <sub>2</sub>				$\rho_{ee}^{(2)}(t) = -i^2I_{ee}(t-t_2)\sum_g V_{eg,2}^- I_{eg}(\tau_{12}) V_{eg,1}^+ \rho_{gg}^{(0)}$
c) $P^{(2)}$				
Q <sub>1</sub> *				$\rho_{gg}^{(2)}(t) = i^2I_{gg}(t-t_2)\sum_e V_{eg,2}^+ I_{eg}^*(\tau_{12}) V_{eg,1}^- \rho_{gg}^{(0)}$
Q <sub>2</sub> *				$\rho_{e'e}^{(2)}(t) = -i^2I_{e'e}(t-t_2)\sum_g V_{eg,2}^+ I_{eg}^*(\tau_{12}) V_{eg,1}^- \rho_{gg}^{(0)}$
d) $P^{(3)}$				
R <sub>4</sub>				$\rho_{e'g}^{(3)}(t) = -i^3I_{e'g}(t-t_3)\sum_g V_{eg,3}^+ I_{gg'}(\tau_{23}) \sum_e V_{eg,2}^- I_{eg}(\tau_{12}) V_{eg,1}^+ \rho_{gg}^{(0)}$
R <sub>1</sub>				$\rho_{eg}^{(3)}(t) = -i^3I_{eg}(t-t_3)\sum_e V_{e'g,3}^+ I_{ee'}(\tau_{23}) \sum_g V_{eg,2}^- I_{eg}(\tau_{12}) V_{eg,1}^+ \rho_{gg}^{(0)}$
e) $P^{(3)}$				
R <sub>3</sub>				$\rho_{e'g}^{(3)}(t) = -i^3I_{e'g}(t-t_3)\sum_g V_{eg,3}^+ I_{gg'}(\tau_{23}) \sum_e V_{eg,2}^+ I_{eg}(\tau_{12}) V_{eg,1}^- \rho_{gg}^{(0)}$
R <sub>2</sub>				$\rho_{e'g}^{(3)}(t) = -i^3I_{e'g}(t-t_3)\sum_e V_{eg,3}^+ I_{e'e}(\tau_{23}) \sum_g V_{eg,2}^+ I_{eg}(\tau_{12}) V_{eg,1}^- \rho_{gg}^{(0)}$

**Figure 2.** Diagrammatic representation (Liouville space couplings, DSFD, and the ladder diagrams) and expressions for the first (a), second (b and c), and third (d and e) order density matrix elements. The formulas indicate how the initial density matrix elements are transformed into higher order elements through interactions with the electric field, operator  $V_{eg,n}^+$  or  $V_{eg,n}^-$ , and field-free propagators,  $I_{eg}(t-t_j)$ , during time intervals  $t_j - t_i$  ( $i, j = 1, 2, \text{ and } 3$ ). In the Liouville space coupling representation, the state of the system is designated by a point in the Liouville space, with the indices corresponding to the ket–bra “axis”. Transitions on the ket are indicated with a vertical line between the points of Liouville space, whereas horizontal lines represent transitions on the bra. In the DSFD, the left and right vertical lines represent the ket and bra, respectively; the applied electric fields are indicated with arrows oriented toward the left if propagating with a negative wave vector and vice versa for a positive wave vector. Time evolves from the bottom to the top of the diagram. In the ladder diagrams, the vibrational manifold of each electronic state is represented by the horizontal lines, the solid and dashed vertical lines correspond to ket and bra interactions, respectively, and time evolves from left to right.

The diagrams of a second-order interaction are depicted in Figure 2 parts b and c for the spatial Fourier components  $(\mathbf{k}_1 - \mathbf{k}_2) \cdot \mathbf{r}$  and  $(-\mathbf{k}_1 + \mathbf{k}_2) \cdot \mathbf{r}$  of the density matrix elements (see Appendix A). Each component corresponds to a different way in which the electric field interacts with the molecules while satisfying the RWA. Diagrams Q<sub>1</sub> and Q<sub>1</sub>\* in Figure 2 parts b and c illustrate the transitions (excitation followed by a deexcitation) taking place either on the ket or the bra. This interaction produces a ground-state population transfer ( $g = g'$ )

and a vibrational coherence ( $g \neq g'$ ),  $\rho_{g'g}^{(2)}(\mathbf{r}, t)$  and  $\rho_{gg'}^{(2)}(\mathbf{r}, t)$ , for each spatial component,  $(\mathbf{k}_1 - \mathbf{k}_2) \cdot \mathbf{r}$  and  $(-\mathbf{k}_1 + \mathbf{k}_2) \cdot \mathbf{r}$ , respectively. Diagrams Q<sub>2</sub> and Q<sub>2</sub>\* in Figure 2 parts b and c show the transitions taking place in both the bra and ket sides. This interaction transfers population ( $e = e'$ ) and generates vibrational coherence ( $e \neq e'$ ) into the excited state,  $\rho_{ee}^{(2)}(\mathbf{r}, t)$  and  $\rho_{e'e}^{(2)}(\mathbf{r}, t)$ , in the  $(\mathbf{k}_1 - \mathbf{k}_2) \cdot \mathbf{r}$  and  $(-\mathbf{k}_1 + \mathbf{k}_2) \cdot \mathbf{r}$  spatial components.

The diagrams of the third-order density matrix for the spatial components  $\mathbf{k}_I \cdot \mathbf{r} = (\mathbf{k}_3 + \mathbf{k}_2 - \mathbf{k}_1) \cdot \mathbf{r}$  and  $\mathbf{k}_{II} \cdot \mathbf{r} = (\mathbf{k}_3 - \mathbf{k}_2 + \mathbf{k}_1) \cdot \mathbf{r}$  (see Appendix A) are depicted in Figure 2 parts d and e, respectively. Each of the terms in eq A5 corresponds to a diagram shown in Figure 2 parts d and e, such that the spatial component  $\mathbf{k}_{II} \cdot \mathbf{r}$  of  $\hat{\rho}^{(3)}(\mathbf{r}, t)$  is given by the DSFD designated by molecular responses (or Liouville-space pathways)  $R_4$  and  $R_1$ . Whereas the component  $\mathbf{k}_I \cdot \mathbf{r}$  is given by the DSFD designated by molecular responses  $R_3$  and  $R_2$ . The Liouville-space pathways  $R_4$  and  $R_3$  result from the polarization of the ground-state population, whereas  $R_1$  and  $R_2$  result from the polarization of excited-state population. Both spatial components of the third-order density matrix elements,  $\mathbf{k}_I$  and  $\mathbf{k}_{II}$ , carry ground- and excited-state dynamics information. We thus have

$$\hat{\rho}^{(3)}(\mathbf{r}, t) = e^{i\mathbf{k}_{II} \cdot \mathbf{r}}(R_4 + R_1) + e^{i\mathbf{k}_I \cdot \mathbf{r}}(R_3 + R_2) + c.c \quad (15)$$

The last column of Figure 2 gives the expressions for  $\hat{\rho}^{(1)}(t)$ ,  $\hat{\rho}^{(2)}(t)$ , and  $\hat{\rho}^{(3)}(t)$  for our two electronic level model system. Each step in the diagrams corresponds to the expression. The dipole interaction with the  $n$ th pulse is indicated by either  $V_{eg,n}^-$  (if carrying a negative wave vector) or by  $V_{eg,n}^+$  (if carrying a positive wave vector; eq 13). The field-free propagation of the ground- and excited-state populations is denoted by  $I_{g'g}(t_3 - t_2)$  and  $I_{e'e}(t_3 - t_2)$ , whereas the electronic coherence propagation is denoted by  $I_{eg}(t_3 - t_2)$ . Note that the third pulse can interact with both ground- and excited-state populations as indicated by the propagators  $I_{g'g}(t_3 - t_2)$  and  $I_{e'e}(t_3 - t_2)$  in each spatial Fourier component of  $\hat{\rho}^{(3)}(t)$ . The components of the density matrix elements are obtained from the product of the interaction operators, in such a way that  $\mathbf{k}_I$  and  $\mathbf{k}_{II}$  in  $\hat{\rho}^{(3)}(t)$  are given by  $V_{eg,1}^- V_{eg,2}^+ V_{eg,3}^+$  and  $V_{eg,1}^+ V_{eg,2}^- V_{eg,3}^+$ , respectively.  $\mathbf{k}_I$  and  $\mathbf{k}_{II}$  correspond to the phase matching directions in which the signal is detected. The wave vector of the emitted electric field is, therefore, either  $\mathbf{k}_I$  or  $\mathbf{k}_{II}$ . The signal detected at  $\mathbf{k}_I$  and  $\mathbf{k}_{II}$  involves different types of molecular response. We will designate each spatial component as a distinct FWM signal. Control of the observed intramolecular dynamics using one of the FWM techniques, can be achieved by choosing a specific pulse sequence that cancels all Liouville-space pathways except one.

### III. Detection Modes for Four-Wave Mixing Signals

Optical signals can be expressed in terms of the Wigner distribution,  $W_S(t, \omega)$ , of the emitted electric field in the  $\mathbf{k}_S$  direction:<sup>81–83</sup>

$$W_S(t, \omega) = \int_{-\infty}^{\infty} d\tau \epsilon_S^*(t - \tau/2) \epsilon_S(t + \tau/2) \exp[i\omega\tau] \quad (16)$$

where

$$E_S(\mathbf{r}, t) = \epsilon_S(t) \mu \rho[-i(\omega_S t - \mathbf{k}_S \cdot \mathbf{r})] + \epsilon_S^*(t) \mu \rho[i(\omega_S t - \mathbf{k}_S \cdot \mathbf{r})] \quad (17)$$

with the subindex  $S = I$  or  $II$  corresponding to the  $\mathbf{k}_I$  or  $\mathbf{k}_{II}$  FWM techniques, respectively. The Wigner spectrogram represents the fraction of the electric field energy contained in a specific time and frequency window  $(t, \omega)$ . The electric field emitted by the sample is proportional to the third-order ensemble-averaged polarization

$$E_S(\mathbf{r}, t) \propto \rho P_S^{(3)}(\mathbf{r}, t) \quad (18)$$

where

$$P_S^{(3)}(\mathbf{r}, t) = Tr[\hat{\mu} \hat{\rho}_S^{(3)}(\mathbf{r}, t)] = \sum_{e,g} \mu_{eg} [\rho_{egS}^{(3)}(\mathbf{r}, t) + \rho_{geS}^{(3)}(\mathbf{r}, t)] = \exp[i\mathbf{k}_S \cdot \mathbf{r}] \sum_{e,g} \mu_{eg} [\rho_{egS}^{(3)}(\tau_{12}, \tau_{23}; t) + c.c] \quad (19)$$

Here  $\hat{\mu}$  is the dipole moment operator and the summation is over the vibrational manifolds of the ground ( $g$ ) and excited state ( $e$ ). The time dependence of the density matrix element  $\rho_{egS}^{(3)}(\tau_{12}, \tau_{23}; t)$  can be factorized, see eq A5, as

$$\rho_{egS}^{(3)}(\tau_{12}, \tau_{23}; t) = \rho_{egS}^{(3)}(\tau_{12}, \tau_{23}) \exp[-i\omega_{eg} t - \gamma_{eg} t] = \rho_{egS}^{(3)}(\tau_{12}, \tau_{23}) \exp[-i(\omega_S + \omega_{egS}) t - \gamma_{eg} t] \quad (20)$$

$\omega_S$  is the frequency of the emitted polarization after three-pulse interaction, with  $\omega_I = (-\omega_1 + \omega_2 + \omega_3)$  and  $\omega_{II} = (\omega_1 - \omega_2 + \omega_3)$  and  $\omega_{egS} \equiv \omega_{eg} - \omega_S$ . The transitions contributing to the polarization result from the interaction between the molecules and the pulses according to the experimental technique  $\mathbf{k}_I$  or  $\mathbf{k}_{II}$  and leading to an emission frequency  $\omega_I$  or  $\omega_{II}$ . The transition frequencies involved in the signal can therefore be expressed as a function of  $\omega_S$  and a linear combination of the vibrational ground- and excited-state frequencies. The time dependence of the emitted electric field in the direction  $\mathbf{k}_S$  is given by

$$\epsilon_S(t) \propto \sum_{e,g} \mu_{eg} \rho_{egS}^{(3)}(\tau_{12}, \tau_{23}) \exp[-i\omega_{eg} t - \gamma t] \quad (21)$$

where we have adopted a simple model for the rate of electronic dephasing (i.e., coherence relaxation)  $\gamma_{eg} = \gamma$ , and the delay times between the pulses are defined as  $\tau_{23} \equiv t_3 - t_2$  and  $\tau_{12} \equiv t_2 - t_1$ . Substituting eq 21 in eq 16, we obtain the following expression for the Wigner spectrogram of the emitted electric field:<sup>81,84</sup>

$$W_S(t, \omega) \propto \int_{-\infty}^{\infty} d\tau \exp[i\omega\tau] \sum_{e_1, g_1} \mu_{e_1 g_1} \rho_{e_1 g_1 S}^{*(3)}(\tau_{12}, \tau_{23}) \exp[(i\omega_{e_1 g_1} - \gamma)(t - \tau/2)] \sum_{e_2, g_2} \mu_{e_2 g_2} \rho_{e_2 g_2 S}^{(3)}(\tau_{12}, \tau_{23}) \exp[(-i\omega_{e_2 g_2} - \gamma)(t + \tau/2)] \quad (22)$$

Performing the integral over  $\tau$  we obtain

$$W_S(t, \omega) \propto \sum_{e_1, g_1} \mu_{e_1 g_1} \mu_{e_2 g_2} \rho_{e_1 g_1 S}^{*(3)}(\tau_{12}, \tau_{23}) \rho_{e_2 g_2 S}^{(3)}(\tau_{12}, \tau_{23}) \exp[2i(\omega_{e_1 g_1} - \omega)t] \exp[-2\gamma t] \quad (23)$$

where the subindices  $e_2 g_2$  are determined by the relation

$$\omega_{e_2 g_2} = 2(\omega - \omega_{e_1 g_1}/2) \quad (24)$$

The instantaneous electric field energy,  $|E_S(t)|^2$ , can be obtained by integrating the Wigner distribution over the frequency

$$|\epsilon_S(t)|^2 \propto \int_{-\infty}^{\infty} d\omega \sum_{e_1, g_1} \mu_{e_1 g_1} \mu_{e_2 g_2} \rho_{e_1 g_1 S}^{*(3)}(\tau_{12}, \tau_{23}) \rho_{e_2 g_2 S}^{(3)}(\tau_{12}, \tau_{23}) \exp[2i(\omega_{e_1 g_1} - \omega)t] \exp[-2\gamma t] \quad (25)$$



The homodyne signal is proportional to the time integral of the instantaneous electric field energy and given by<sup>13</sup>

$$S_S = \int_{-\infty}^{\infty} dt [P_S^{(3)}(t)]^2 \propto \int_{-\infty}^{\infty} dt |\epsilon_S(t)|^2 \quad (26)$$

The frequency-dispersed homodyne signal is obtained when the instantaneous field energy is measured with an ideal detector centered at a specific frequency,  $\Phi(\omega, \omega_D) = \delta(\omega - \omega_D)$ . The signal in the direction  $\mathbf{k}_S$  is then given by

$$S_S(\tau_{12}, \tau_{23}, \omega_D) \propto \int_{-\infty}^{\infty} dt \int_{-\infty}^{\infty} d\omega \sum_{e_1, g_1} \mu_{e_1, g_1} \mu_{e_2, g_2} \rho_{e_1, g_1, S}^{*(3)}(\tau_{12}, \tau_{23}) \rho_{e_2, g_2, S}^{(3)}(\tau_{12}, \tau_{23}) \delta(\omega - \omega_D) \exp[2i(\omega_{e_1, g_1} - \omega)t] \exp[-2\gamma t] \quad (27)$$

After performing the integral over the frequency, the frequency-gate function fixes the value of  $\omega$  to  $\omega = \omega_D$ , whereas the time integral gives

$$S_S(\tau_{12}, \tau_{23}, \omega_D) \propto \sum_{e_1, g_1} \mu_{e_1, g_1} \mu_{e_2, g_2} \rho_{e_1, g_1, S}^{*(3)}(\tau_{12}, \tau_{23}) \rho_{e_2, g_2, S}^{(3)}(\tau_{12}, \tau_{23}) \times \frac{\gamma}{2(\gamma^2 + (\omega_{e_1, g_1} - \omega_D)^2)} \quad (28)$$

The dominant contribution to  $S_S(\tau_{12}, \tau_{23}, \omega_D)$  comes when the central frequency of the detector is equal to one of the transition frequencies involved in the sum,  $\omega_D = \omega_{e_1, g_1}$ . Then, when  $\omega = \omega_D = \omega_{e_1, g_1}$ , the subscripts  $e_2, g_2$  adopt the value  $e_2, g_2 = e_1, g_1$  (see eqs 22–23) and the frequency dispersed homodyne signal in the detection direction  $\mathbf{k}_S$  is given by

$$S_S(\tau_{12}, \tau_{23}, \omega_D = \omega_{e_1, g_1}) \propto \frac{1}{2\gamma} |\mu_{e_1, g_1} \rho_{e_1, g_1, S}^{(3)}(\tau_{12}, \tau_{23})|^2 \quad (29)$$

These signals constitute various examples of multidimensional spectroscopies.<sup>23,85–87</sup> Different two-dimensional (2D) signals can be obtained when one of the three variables in eq 29 is held fixed. When one of the delay times between a pair of pulses is fixed, the 2D-signal contains information about the dynamics of the different transitions that contribute to the FWM signal as a function of the scanning time. Scanning time versus frequency resolved signals in four wave mixing in vapor iodine have been studied by the Dantus and Kiefer groups.<sup>59,61,63,88</sup> This information indicates which transitions are activated with a specific pulse sequence and can be applied to study IVR. When the detection frequency  $\omega_D$  is fixed at a specific transition frequency, we obtain a 2D plot with two temporal axes: fixed time and scanning time. At specific values of the fixed time delay, the signal is modulated by ground or excited-state dynamics as a function of the scanning time.<sup>73,89</sup> The fixed times correspond to half periods of the wave packet motion at a given energy level of the ground or excited potential curve and are proportional to the potential width at that energy. The time delay allows one to manipulate the microscopic and macroscopic coherence that modulates the observed signal.<sup>89</sup> A collection of transition frequency plots will map the anharmonicity of the potentials. The homodyned frequency dispersed signal can be calculated by substituting eq A5 into eq 29. The signal in direction  $\mathbf{k}_I$  is then given by

$$S_I(\tau_{12}, \tau_{23}, \omega_D = \omega_{eg}) = |\mu_{eg} A_I(\tau_{12}, \tau_{23}, \omega_{eg})|^2 \quad (30)$$

where

$$A_I(\tau_{12}, \tau_{23}, \omega_{eg}) \propto \sum_g V_{eg',3}^+ I_{g',g}(\tau_{23}) \sum_{e'} V_{e',g,2}^+ I_{e',g}(\tau_{12}) V_{e',g,1}^- \rho_{g',g'}^{(0)} + \sum_{e'} V_{e',g,3}^+ I_{ee'}(\tau_{23}) \sum_g V_{eg',2}^+ I_{e',g}(\tau_{12}) V_{e',g,1}^- \rho_{g',g'}^{(0)} \quad (31)$$

The summation over the indices  $e'$  and  $g'$  corresponds to the contributions of the vibrational manifolds of the excited and ground electronic states, respectively. The homodyne frequency-dispersed signal for the spatial component  $\mathbf{k}_{II}$  is given by

$$S_{II}(\tau_{12}, \tau_{23}, \omega_D = \omega_{eg}) = |\mu_{eg} A_{II}(\tau_{12}, \tau_{23}, \omega_{eg})|^2 \quad (32)$$

where

$$A_{II}(\tau_{12}, \tau_{23}, \omega_{eg}) \propto \sum_g V_{eg',3}^+ I_{g',g}(\tau_{23}) \sum_{e'} V_{e',g,2}^- I_{e',g}(\tau_{12}) V_{e',g,1}^+ \rho_{gg}^{(0)} + \sum_{e'} V_{e',g,3}^+ I_{ee'}(\tau_{23}) \sum_{g'} V_{e',g',2}^- I_{eg'}(\tau_{12}) V_{e',g,1}^+ \rho_{g',g'}^{(0)} \quad (33)$$

The homodyne signal can be obtained combining eqs 26 and 19:

$$S_S(\tau_{12}, \tau_{23}) = \int_{-\infty}^{\infty} dt [P_S^{(3)}(\tau_{12}, \tau_{23}; t)]^2 = \int_{-\infty}^{\infty} dt \left[ \sum_{e,g} P_{egS}^{(3)}(\tau_{12}, \tau_{23}; t) \right]^2 \quad (34)$$

where the summation is over the ground- and excited-state vibrational manifolds. The third-order polarization for each transition is given by

$$P_{egS}^{(3)}(\tau_{12}, \tau_{23}; t) \equiv \mu_{eg} (\rho_{egS}^{(3)}(\tau_{12}, \tau_{23}; t) + \rho_{geS}^{(3)}(\tau_{12}, \tau_{23}; t)) \quad (35)$$

Then

$$S_S(\tau_{12}, \tau_{23}) = \sum_{e,g} \int_{-\infty}^{\infty} dt [P_{egS}^{(3)}(\tau_{12}, \tau_{23}; t)]^2 + 2 \sum_{e_1, g_1, e_2, g_2} \int_{-\infty}^{\infty} dt P_{e_1, g_1, S}^{(3)}(\tau_{12}, \tau_{23}; t) P_{e_2, g_2, S}^{(3)}(\tau_{12}, \tau_{23}; t) = \sum_{e,g} \frac{1}{2\gamma} |\rho_{egS}^{(3)}(\tau_{12}, \tau_{23})|^2 + \sum_{e_1, g_1, e_2, g_2} \frac{\gamma}{(\gamma^2 + (\omega_{e_1, g_1} - \omega_{e_2, g_2})^2)} (\rho_{e_1, g_1, S}^{(3)}(\tau_{12}, \tau_{23}) \rho_{e_2, g_2, S}^{*(3)}(\tau_{12}, \tau_{23}) + c.c.) \quad (36)$$

Here the RWA has been invoked where highly oscillatory contributions are neglected. The second term represents a macroscopic interference of polarizations from different molecules.<sup>73,89</sup> This type of interference arises because the homodyne detection is quadratic in the emitted polarization and will be present in any homodyne signal. This interference effect is measurable if the relaxation time ( $1/\gamma$ ) is comparable with ground or excited-state vibrational periods. The interference term is given by the sum of terms that oscillate with a linear combination of the ground- and excited-state vibrational fre-

quencies (see Appendix B), and its contribution can be expressed as

$$\begin{aligned} \rho_{e_1g_1s}^{(3)}(\tau_{12}, \tau_{23}) \rho_{e_2g_2s}^{*(3)}(\tau_{12}, \tau_{23}) = \\ \sum_{ij} S_{R_i(e_1g_1); R_j(e_2g_2)}(\tau_{12}, \tau_{23}) \equiv \\ \sum_n A_{ns}(e_1, g_1, e_2, g_2; \tau_{12}, \tau_{23}) \cos((n_e \omega_e + n_g \omega_g) \tau_{23}) + \\ B_{ns}(e_1, g_1, e_2, g_2; \tau_{12}, \tau_{23}) \cos((n_e \omega_e + n_g \omega_g) \tau_{12}) \end{aligned} \quad (37)$$

where  $S_{R_i(e_1g_1); R_j(e_2g_2)}(\tau_{12}, \tau_{23})$  terms denote the interference of polarizations arising from molecules excited with Liouville pathways  $R_i(e_1g_1)$  and  $R_j(e_2g_2)$ .  $R_i(e_1g_1)$  represents the contribution of the Liouville pathway  $R_i$  to the electronic coherence  $\rho_{e_1g_1s}^{(3)}$ . If the signal is detected in the  $\mathbf{k}_I$  direction,  $i, j = 2, 3$ , whereas for  $\mathbf{k}_{II}$ ,  $i, j = 1, 4$ . Expressions for the coefficients  $A_{ns}(e_1, g_1, e_2, g_2, \tau_{12}, \tau_{23})$ ,  $B_{ns}(e_1, g_1, e_2, g_2, \tau_{12}, \tau_{23})$ ,  $n_e$ , and  $n_g$  can be obtained from the expressions of Appendix B. From eqs 30–33, we can calculate the FWM signal if the spectral intensity of the pulses, the initial distribution of the vibrational levels in ground state, and few molecular parameters are known. In particular, for ultrafast measurements in the gas phase, where the relaxation processes are slow compared to the vibrational period, the molecular parameters are reduced to the vibronic dipole couplings,  $\mu_{eg}$ .

A joint time-frequency representation of the nonlinear response and signals was developed and applied in refs 70–73, 82–84, and 90. The joint time-frequency resolved signals and analysis of various coherences in four wave mixing in vapor iodine have been studied by Apkarian and co-workers.<sup>91</sup>

If a detector with a short temporal window is used, one can measure the time-gated signal. In this case, the integral in eq 26 should be taken within the specified time-gate window. The window is achieved experimentally using a Kerr-gate.<sup>92</sup> Mathematically a Gaussian function can be introduced to simulate the gate.

Improvements in the signal-to-noise ratio can be achieved using heterodyne detection. The heterodyne signal is linear in the weak nonlinear polarization improving the sensitivity of the measurement. In this detection mode, a new (local oscillator) field with wave vector  $\mathbf{k}_{LO}$  ( $\mathbf{k}_{LO} = \mathbf{k}_S$ ), carrier frequency  $\omega_{LO}$ , and phase  $\phi_{LO}$  is applied at time  $\tau'$ . The signal results from the superposition of the local oscillator field and the third-order polarization:<sup>13</sup>

$$S_{HS}(\mathbf{r}; \tau_{12}, \tau_{23}) = \int_{-\infty}^{\infty} dt E_{LO}(\mathbf{r}, t) P_S^{(3)}(\mathbf{r}, t; \tau_{12}, \tau_{23}) = S_{HS}(\tau_{12}, \tau_{23}) \exp[i(\mathbf{k}_{LO} + \mathbf{k}_S) \cdot \mathbf{r}] \quad (38)$$

where

$$E_{LO}(\mathbf{r}, t) = \epsilon_{LO}(t - \tau') \exp[i\mathbf{k}_{LO} \cdot \mathbf{r} - i\omega_{LO}t - i\phi_{LO}] + c.c. \quad (39)$$

The signal amplitude is then given by

$$S_{HS}(\tau_{12}, \tau_{23}) = 2 \text{Im}[\exp[i\phi_{LO}] \int_{-\infty}^{\infty} dt \epsilon_{LO}^*(t - \tau') \exp[i\omega_{LO}t] P_S^{(3)}(t; \tau_{12}, \tau_{23})] \quad (40)$$

The phase of the local oscillator field can be used to separate the real and imaginary components of the polarization  $P_S^{(3)}(\mathbf{r}, t; \tau_{12}, \tau_{23})$ , which give the phase of the signal field. The heterodyne signal as a function of the third-order density matrix can be obtained by calculating the third-order polarization from

eq 19 and substituting in eq 40:

$$S_{HS}(\tau_{12}, \tau_{23}) = 2 \text{Im}[\sum_{e,g} \mu_{eg} \int_{-\infty}^{\infty} dt \epsilon_{LO}^*(t - \tau') \exp[i(\omega_{LO}t + \phi_{LO})] (\rho_{egs}^{(3)}(t; \tau_{12}, \tau_{23}) + c.c.)] \quad (41)$$

Performing the time integration we obtain

$$S_{HS}(\tau_{12}, \tau_{23}) = 2 \text{Re}[\exp[i\phi_{LO}] \exp[(i\omega_{LO} - \gamma)(\tau' - t_3)] \sum_{e,g} \mu_{eg} \tilde{\epsilon}_{LO}^*(\omega_{LO} - \omega_{eg} - i\gamma) \exp[(-i\omega_{eg})(\tau' - t_3)] \rho_{egs}^{(3)} \times (\tau_{12}, \tau_{23}) + \mu_{eg} \tilde{\epsilon}_{LO}^*(\omega_{LO} + \omega_{eg} - i\gamma) \exp[(+i\omega_{eg})(\tau' - t_3)] \rho_{egs}^{(3)}(\tau_{12}, \tau_{23})] \quad (42)$$

where  $\tilde{\epsilon}_{LO}^*(\omega)$  is the Fourier transform of the temporal envelop of the local oscillator field. Note that this expression for the heterodyne signal contains no interference term. In the limit of small relaxation rate ( $\gamma \rightarrow 0$ ), if the frequency of the local oscillator electric field is equal to one of the transition frequency,  $\omega_{LO} = \omega_{eg}$ , the RWA can be applied and only one term in eq 42 will give a significant contribution to the signal. We then obtain the spectrally dispersed heterodyned signal

$$S_{HS}(\tau_{12}, \tau_{23}, \omega_{LO} = \omega_{eg}) = 2 \text{Re}[\exp[i\phi_{LO} - \gamma(\tau' - t_3)] \times \tilde{\epsilon}_{LO}^*(\omega_{LO} - \omega_{eg}) \rho_{egs}^{(3)}(\tau_{12}, \tau_{23})] \quad (43)$$

This setup, requiring two pairs of phase locked pulses (1,2 and 3,LO), can be used to determine the phase of the polarizations arising from individual transitions by varying the phase of the local field. The additional sensitivity, the absence of interference, and the fact that the phase of the polarization can be obtained make the extra experimental effort involved in heterodyne detection worthwhile.<sup>93–97</sup> Heterodyne detected FWM is not common in the gas phase.

#### IV. Controlling the Four-Wave Mixing Molecular Response

Different levels of control can be achieved by manipulating the experimental parameters that generate the  $S_I$  and  $S_{II}$  signals.<sup>73,89</sup>  $S_I$  arises from the molecular Liouville Space pathways  $R_2$  and  $R_3$ , whereas  $S_{II}$  arises from  $R_1$  and  $R_4$ . Signals corresponding to the first group decay with a homogeneous relaxation rate, whereas those corresponding to the second group decay with both inhomogeneous and homogeneous relaxation processes.<sup>21,24</sup> A schematic representation of the repurposing process that leads to the cancellation of the inhomogeneous decay in  $S_I$  signals is presented in Figure 3. In this case, the first pulse establishes a bra electronic coherence,  $\rho_{ge}^{(1)}(t)$ , (first interaction with  $-\mathbf{k}_I \cdot \mathbf{r}$ ) that evolves during a time  $t = \tau_{12}$ . The third pulse produces a ket electronic coherence,  $\rho_{eg}^{(3)}(t)$ , that evolves “backwards” in time with respect to  $\rho_{ge}^{(1)}(t)$ . The third-order polarization, results from the “reversed” coherence and reaches its maximum at a time  $t = 2\tau_{12} + \tau_{23}$ . The evolution of the bra and ket coherences is represented in Figure 3 by the dashed and solid lines, respectively. The PE pulse sequence is very similar to the Hahn spin-echo pulse sequence used in magnetic resonance spectroscopy.<sup>98</sup> In the SPE sequence, the time between the first two pulses is different from zero and the initial coherence is allowed to evolve in time. The coherence evolution time is useful to determine inhomogeneous dephasing, a measurement of particular importance to determine the structure and surrounding environment of molecules. In mag-

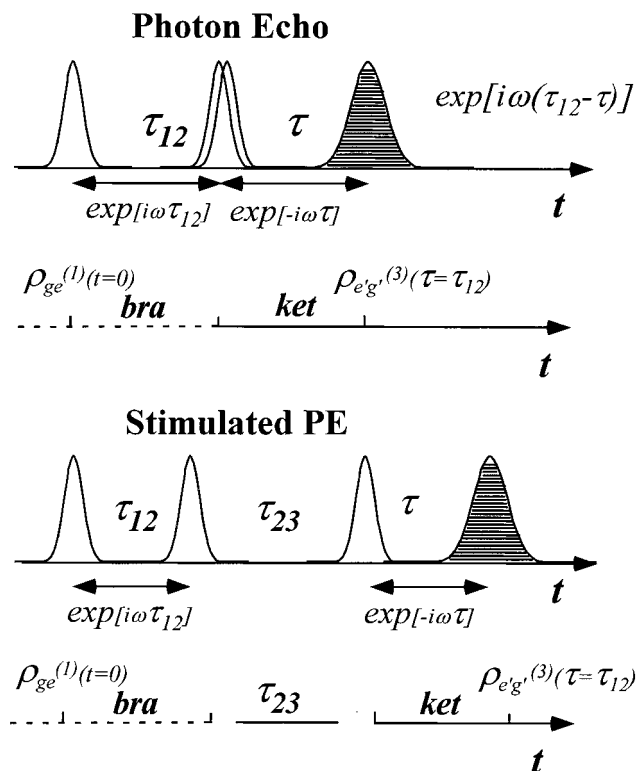


**Figure 3.** Schematic representation of the rephasing mechanism in  $S_1$  signals. In the photon echo pulse sequence, the first electric field interaction creates a coherence, represented here by the first-order density matrix elements  $\rho_{ge}^{(1)}$  with evolution on the bra (dashed line). After two more electric field interactions, the third-order density matrix elements  $\rho_{e'g'}^{(3)}$  evolve on the ket (solid line). The photon echo amplitude reaches its maximum after  $\tau_{13}$  at a time equal to the time delay between the first two pulses,  $\tau = \tau_{12}$ . In the stimulated photon echo pulse sequence, the population and the vibrational coherence are allowed to propagate for a time  $\tau_{23}$ , the time delay between the last two pulses. This evolution is represented by a propagation of the bra (dashed line) and the ket (solid line) on the time axis. Again, the stimulated photon echo amplitude reaches its maximum when  $\tau = \tau_{12}$ .

netic resonance, the nuclear Overhauser effect spectroscopy (NOESY) pulse sequence is analogous to the SPE sequence.<sup>99</sup>

The first level of control is aimed at separating the  $S_1$  and  $S_{II}$  FWM signals. This can be achieved by selecting signals for which the first interaction is either on the bra or on the ket. This task is relatively simple when noncollinear pulses are used where  $S_1$  and  $S_{II}$  signals have distinct phase matching directions. The second level of control is aimed at isolating a single pathway ( $R_1$ ,  $R_2$ ,  $R_3$  or  $R_4$ ) from  $S_1$  or  $S_{II}$  signals. Here, the molecular dynamics of the system can usually be used to minimize the contribution of the undesirable responses.<sup>73</sup> Molecular responses can be minimized when the time delay between the pulses of a pair  $\pm(\mathbf{k}_i - \mathbf{k}_j)$  ( $i, j = 1, 2$ , and 3) acting on the same side of the diagram is out-of-phase with respect to the vibrational period of the excited electronic state. Information about the vibrational period of the excited electronic state can be obtained from a four-wave mixing technique in which two pulses overlap in time (photon echo or transient grating), as shown in the next section. This suppression mechanism of the molecular response is related to the pump–dump control method<sup>7</sup> in that it takes advantage of a time-dependent transition probability as the wave packet moves in and out of the optically coupled region. In such a way,  $R_1$  can be suppressed by controlling the time delay  $\tau_{23}$  (minimizing the probing step),  $R_2$  with  $\tau_{13}$  (minimizing the probing step),  $R_3$  with  $\tau_{12}$  (minimizing the transition that creates a population), and  $R_4$

with  $\tau_{12}$  (minimizing the transition that creates a population) or  $\tau_{23}$  (minimizing the probing step). The selection of one pathway from  $S_1$  or  $S_{II}$  leads to the observation of ground or excited-state dynamics<sup>19,60,61,63,73</sup> because the molecular response that contributes to each signal corresponds to the polarization of ground or excited-state populations.

Generating two or more sets of wave packets in the excited state that interfere destructively provides an additional possibility for suppressing nonlinear molecular responses.<sup>89</sup> This can be achieved when two or more vibrational levels are initially populated in the ground state and their Franck–Condon factors with the excited state are nearly identical. Under these circumstances, each laser pulse creates an excited-state wave packet from each of the ground-state levels. The first pulse generates two wave packets that are in phase. However, when the second pulse is timed such that it is out of phase with the ground-state vibrational period, the wave packets it generates are out of phase and the signals interfere destructively. This situation can be achieved for the  $R_1$  and  $R_2$  responses.<sup>89</sup> Control methods based on quantum mechanical interference using ground state hot bands as discussed here are more powerful when the initial population is equally distributed among a few initial ground-state vibrational levels.<sup>89</sup> These types of control do not require phase matching or phase locking.

To illustrate the selection of individual molecular responses by controlling the time delay between the pulses, we have calculated the  $S_1$  and  $S_{II}$  FWM signals from a simplified model. The model consists of two electronic states with two vibrational level each, vibrational levels  $|g\rangle$  and  $|g'\rangle$  in the ground state and  $|e\rangle$  and  $|e'\rangle$  in the excited state. The vibrational frequency of the ground and excited state are  $\omega_g = (\bar{E}_{g'} - \bar{E}_g)/\hbar$  and  $\omega_e = (\bar{E}_{e'} - \bar{E}_e)/\hbar$ , respectively. This model has the minimum number of levels required to obtain vibrational dynamics information corresponding to each electronic state. The dipole moments  $\mu_{eg} = \mu_{e'g} = -1$  and  $\mu_{e'g'} = \mu_{eg'} = 1$  were determined according to the Condon approximation  $\mu_{eg} = \mu\langle e|g\rangle$ , where  $\mu$  is the electronic transition dipole moment between the ground and  $\langle e|g\rangle$  is the overlap integral between the ground- and excited-state vibrational eigenfunctions. Initially, the molecules are at thermal equilibrium in the ground electronic state. We define the population difference variable  $w \equiv \rho_{g'g'}^{(0)} - \rho_{gg}^{(0)}$ . Then, the FWM homodyne signal in the  $\mathbf{k}_I$  detection direction is given by

$$S_I(\tau_{12}, \tau_{23}) \propto \frac{1}{\gamma} [(1 + w^2) + (1 + w^2) \cos(\omega_g(\tau_{12} + \tau_{23}))] \times [1 + \cos(\omega_e \tau_{12})] + \frac{1}{\gamma} [(1 + w^2) + (1 - w^2) \cos(\omega_g \tau_{12})] \times [1 + \cos(\omega_e(\tau_{12} + \tau_{23}))] + S_{\text{int},I} \quad (44)$$

The term  $S_{\text{int},I}$  can result from the interference between the Liouville pathways ( $R_2$  and  $R_3$ ) of different molecules or from a quantum superposition of pathways in the same molecule:

$$S_{\text{int},I}(\tau_{12}, \tau_{23}) = S_{R_2;R_2}(\tau_{12}, \tau_{23}) + S_{R_2;R_3}(\tau_{12}, \tau_{23}) + S_{R_3;R_2}(\tau_{12}, \tau_{23}) + S_{R_3;R_3}(\tau_{12}, \tau_{23}) \quad (45)$$

The signal in the  $\mathbf{k}_{II}$  detection direction is given by

$$S_{II}(\tau_{12}, \tau_{23}) \propto \frac{1}{\gamma} [(1 + w^2) + (1 + w^2) \cos(\omega_e \tau_{12})] \times [1 + \cos(\omega_g \tau_{23})] + \frac{1}{\gamma} [(1 + w^2) + (1 - w^2) \cos(\omega_g \tau_{12})] \times [1 + \cos(\omega_e \tau_{23})] + S_{\text{int},II} \quad (46)$$

The interference term for  $S_{II}$  is given by the interference between the Liouville pathways ( $R_1$  and  $R_4$ ):

$$S_{\text{int},II}(\tau_{12}, \tau_{23}) = S_{R_1;R_1}(\tau_{12}, \tau_{23}) + S_{R_1;R_4}(\tau_{12}, \tau_{23}) + S_{R_4;R_1}(\tau_{12}, \tau_{23}) + S_{R_4;R_4}(\tau_{12}, \tau_{23}) \quad (47)$$

$S_{R_i;R_i}(\tau_{12}, \tau_{23})$  ( $i = 1, 2, 3$ , and  $4$ ) represents the interference that results from the polarization of molecules that are excited according to  $R_i$  Liouville pathway with coherences coupled to a different excited-state vibrational level.  $S_{R_i;R_j}(\tau_{12}, \tau_{23})$  ( $i \neq j$ ) represents the interference that results from the polarization of molecules excited according to  $R_i$  and  $R_j$  Liouville pathways. Expressions for the interference terms are given in Appendix B.

In eqs 44–47, we can identify terms that depend solely on the ground- or the excited-state vibrational frequencies. In particular, the time delays between the pulses ( $\tau_{12}$ ,  $\tau_{23}$  or  $\tau_{13} = \tau_{12} + \tau_{23}$ ) can be chosen such that only one term oscillating with either  $\omega_g$  or  $\omega_e$  contributes to  $S_I$  or  $S_{II}$  as a function of another variable time delay.<sup>63,89,100</sup>  $S_I$  is controlled by the delay times  $\tau_{12}$  and  $\tau_{13}$ , whereas  $S_{II}$  is controlled by  $\tau_{12}$  and  $\tau_{23}$ . When  $\tau_{12} = (2\pi/\omega_e)(n + 1/2)$ , both  $S_I$  and  $S_{II}$  do not depend on  $\omega_g$  ( $R_3$  and  $R_4$  are suppressed for  $S_I$  and  $S_{II}$ , respectively), and the signal is modulated as a function of  $\tau_{23}$  by the excited-state dynamics. When  $\tau_{12} = (2\pi/\omega_g)(n + 1/2)$ ,  $S_I$  and  $S_{II}$  are mainly modulated by the ground-state vibrational motion with an additional contribution from excited-state motion, proportional to  $w^2$ . When  $\tau_{23} = (2\pi/\omega_e)(n + 1/2)$ ,  $S_{II}$  does not depend on  $\omega_g$  ( $R_4$  is suppressed), and the signal is modulated as a function of  $\tau_{12}$  by the excited-state dynamics. When  $\tau_{23} = (2\pi/\omega_g)(n + 1/2)$ ,  $S_{II}$  is modulated by the ground-state vibrational motion ( $R_1$  is suppressed). Similarly, when  $\tau_{13} = (2\pi/\omega_e)(n + 1/2)$ ,  $S_I$  is modulated as a function of  $\tau_{12}$  by the excited-state dynamics ( $R_3$  is suppressed). When  $\tau_{13} = (2\pi/\omega_g)(n + 1/2)$ ,  $S_I$  is modulated by the ground-state vibrational motion ( $R_2$  is suppressed). The excited-state contribution can be suppressed when the delay time  $\tau_{12} = (2\pi/\omega_e)(n + 1/2)$ . The wavelength of the laser pulses can be chosen to isolate the vibrational motion in the ground state. In these experiments, the wavelength of the second pulse can only induce deexcitation, thereby restricting the signal to CARS transitions and the creation of populations and vibrational coherences in the ground-state only.<sup>51,54,65,91,101–104</sup>

## V. Four Wave Mixing with Three Well-separated Pulses

Three nonoverlapping pulses arranged in the forward-box geometry can lead to signal in two phase matching directions,  $\mathbf{k}_I$  and  $\mathbf{k}_{II}$ , (the position of the detector does not change only the time order of the pulses). When the  $\mathbf{k}_I$  signal is detected, fixing  $\tau_{12}$  and varying  $\tau_{23}$  gives stimulated photon echo (SPE) measurements, whereas fixing  $\tau_{13}$  and varying  $\tau_{12}$  gives mode suppression measurements.<sup>105,106</sup> SPE will show excited-state beats for appropriate values for  $\tau_{12}$ , whereas mode suppression measurements will display ground-state dynamics for specific values of  $\tau_{13}$ .<sup>89</sup> Measuring the peak shift of the SPE signal with respect to  $\tau_{23}$  in solution gives information about solvation dynamics.<sup>107–109</sup>

The virtual echo (VE) technique involves detection of the  $\mathbf{k}_{II}$  signal, fixing  $\tau_{12}$  and scanning the time  $\tau_{23}$ .<sup>110</sup> This technique is also known by other names in the literature<sup>111,112</sup> and is related to the coherent anti-Stokes and coherent Stokes Raman scattering (CARS and CSRS) techniques when laser pulses of different wavelengths are used. Here we show that ground- or excited-state dynamics can be observed with degenerate laser pulses depending on the value of  $\tau_{12}$  ( $\tau_{23}$ ).<sup>19,60,61,63,73</sup> The time

delay between the first two pulses has also been used to enhance the CARS signal in related experiments by Materny and Knopp.<sup>57,113</sup> In Table 1, we summarize the characteristics of FWM signals obtained with three nonoverlapping pulses. The molecular responses that contribute to the signal, the pulse sequence, and an expression for the signals in terms of the third-order polarization for homodyne and heterodyne detection, are given for each case. These expressions neglect relaxation, which for gas-phase samples are slow compared to the vibrational dynamics. The delay time between the pulses are designated as  $\tau_{ij}$  ( $i, j = 1, 2$ , and  $3$ ). Heterodyne signals are obtained as a function of the scanning times and the delay time of the local oscillator field,  $\tau'$ .

To demonstrate the molecular response selection mechanisms discussed in the previous section, we present degenerate three-pulse FWM experiments in gas-phase  $I_2$ . Details of the experimental setup can be found elsewhere.<sup>19,58,63,73</sup> In resonant three-pulse FWM experiments at 620 nm, the iodine molecules undergo transitions between the ground state and the B excited state. On the basis of the Franck–Condon factors, excitation at 620 nm couples the vibrational levels 2nd–5th in the ground state with 7th–13th in the excited state.<sup>69</sup> In Figure 4, we show experimental VE and SPE measurements obtained with three nonoverlapping pulses. The transients along with their fast Fourier transform are included in each case. In Figure 4a, we present VE for fixed  $\tau_{12} = 460$  fs,  $\tau_{12} = {}^{3/2}(2\pi/\omega_e)$ , showing beats modulated with a 307 fs period, corresponding to excited-state motion. The transient shown in Figure 4b was obtained with  $\tau_{12} = 614$  fs,  $\tau_{12} = 2(2\pi/\omega_e)$ , presenting ground-state oscillations with a 160 fs period. The slow modulation component ( $\sim 3$  ps) corresponds to the initial rotational dephasing. The rotational component arises from the inhomogeneous dephasing characteristic to  $\mathbf{k}_{II}$  signals. In Figure 4c, we present SPE for fixed time delay  $\tau_{12} = 460$  fs displaying beats modulated with excited-state motion, whereas the SPE transient for a fixed time delay  $\tau_{12} = 614$  fs (Figure 4d) contains a mixture of ground- and excited-state dynamics. Selection of the  $R_2$  response requires specific values of  $\tau_{13}$  and not  $\tau_{12}$ . Note that the VE signal is as intense as the SPE signal. This situation is characteristic of gas-phase systems, in which the collisional and rotational dephasing are slow compared with the vibrational motion.

Two-dimensional data obtained with  $\mathbf{k}_{II}$  detection are shown in Figure 5. We present a frequency dispersed signal, when  $\tau_{12}$  is fixed and the data is collected as a function of  $\tau_{23}$  and the detector frequency,  $\omega_D = \omega_{eg}$ . This signal arises from the polarization of the sample, detected at the wavelengths indicated on the vertical axis of the plot, as a function of the time delay  $\tau_{23}$ . The lighter regions correspond to higher signal intensity. Figure 5a shows experimental and theoretical data when  $\tau_{12} = 614$  fs. The frequency components oscillate with 160 fs period, corresponding to ground-state vibration. Note that near 628 nm the transient is modulated by the excited-state vibrational motion, indicating a contribution from a population in the excited state. The presence of excited-state dynamics is because anharmonicity causes differences in the wave packet dynamics such that the time delay  $\tau_{12}$  cannot suppress all of the coherent contributions. Simulations for a multilevel system using eq 23 are also included. Experimental and theoretical data for  $\tau_{12} = 460$  fs is shown in Figure 5b. The frequency components of the two-dimensional spectra oscillate with the vibrational period of the excited state. In both cases, the simulation neglects relaxation and rotational contributions to the dynamics. The simulations include Franck Condon factors and spectroscopic

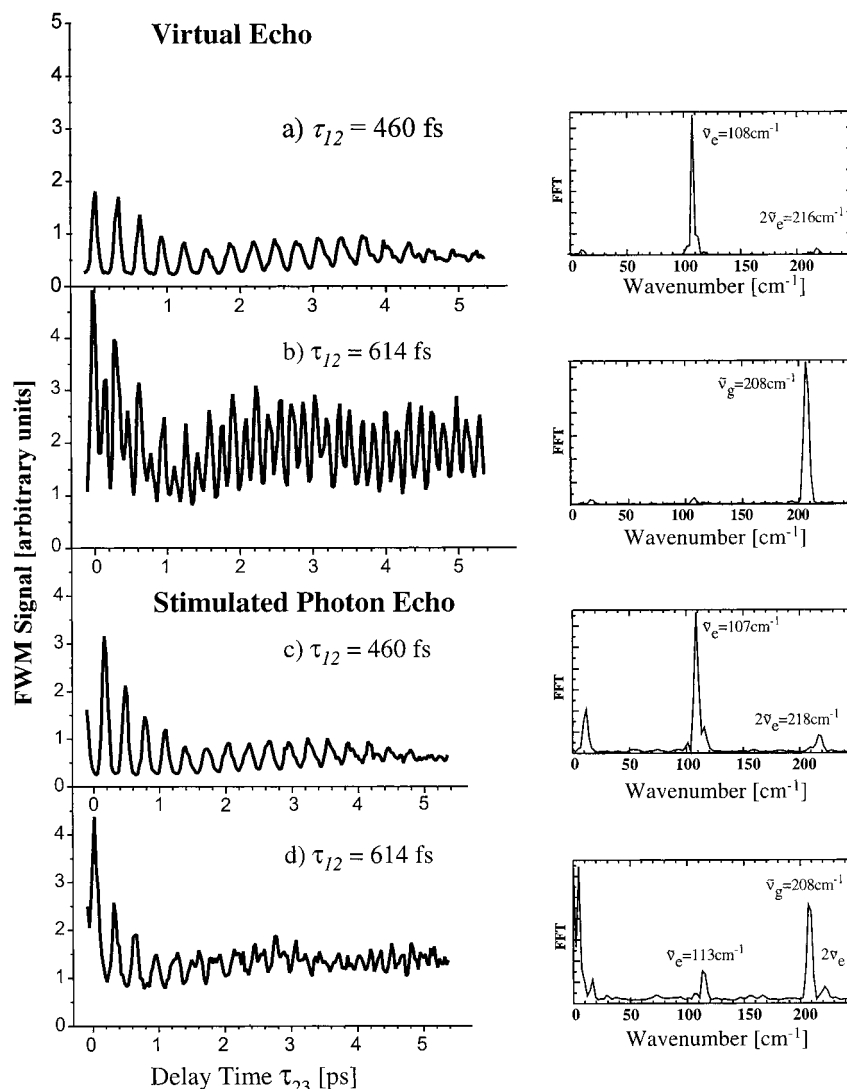


**Figure 4.** Experimental transients and their Fourier transform for processes requiring a fixed delay time between the first two pulses, for the B–X transition of  $I_2$ . With the virtual echo pulse sequence the fixed time delay between the first two pulses,  $\tau_{12}$ , can be chosen to maximize or minimize the transfer of population between the electronic states. VE transients for time delays (a)  $\tau_{12} = 460$  fs and (b)  $\tau_{12} = 614$  fs are shown, for which we selectively obtain excited or ground-state oscillations as shown by their FFT, respectively. Transients obtained with stimulated photon echo pulse sequence with time delay (c)  $\tau_{12} = 460$  fs and (d)  $\tau_{12} = 614$  fs and their FFT are also shown. Notice that SPE does not allow the same control based on  $\tau_{12}$  as observed for VE pulse sequence (see text).

data of the 2nd–5th vibrational levels of the ground state and the 6th–15th vibrational levels in the excited state from refs 69 and 114 with pulses having  $230\text{ cm}^{-1}$  spectral widths. The calculations are in excellent agreement with experiment. This close agreement demonstrated the power of the density matrix method for the calculation of coherent spectroscopic signals. This detection mode, which disperses the signal in frequency, can be viewed as the Fourier transform of the two-dimensional time gating technique.<sup>115,116</sup>

Frequency dispersed signals can be used to gain a better understanding of the effect of chirp in laser excitation. Chirped pulses have been shown to enhance multiphoton excitation and the yield of photochemical reactions.<sup>60,117,118</sup> Chirp excitation leads to a chirped wave packet, one that has the phase structure imparted by the pulse. When chirped pulses are in FWM experiments and that signal is frequency dispersed, it is possible to observe the chirped wave packet motion. The effects of chirp in FWM have been explored by the Dantus group.<sup>59,61,63</sup> The incorporation of computer controlled pulse shapers, which can arbitrarily control the phase and amplitude of different frequen-

cies within a pulse, into three-pulse FWM measurements is already underway.<sup>119–123</sup>

## VI. Four Wave Mixing with One Pair of Overlapping Pulses

When two pulses overlap in time, the previous classification based on the time ordering of the pulses, as  $\mathbf{k}_I$  and  $\mathbf{k}_{II}$ , is not valid anymore.<sup>13,73,124</sup> Therefore, a different classification was introduced in ref 124. Sequences of three noncollinear pulses, in which the temporal overlapping pair is preceded by a single pulse, yield photon echo (PE) signals at the phase-matching direction  $\mathbf{k}_{PE} = -\mathbf{k}_1 + \mathbf{k}_2 + \mathbf{k}'_2$  and reverse transient grating (RTG) signals at  $\mathbf{k}_{RTG} = \mathbf{k}_1 + -\mathbf{k}_2 + \mathbf{k}'_2$  (overlapping pulses have the same subscript, where the apostrophe indicates noncollinear pulses).<sup>63,73</sup> Although if the single pulse is preceded by the temporal overlapping pair, a reverse photon echo (RPE) signal is detected at the phase-matching direction  $\mathbf{k}_{RPE} = \mathbf{k}_1 + \mathbf{k}'_1 - \mathbf{k}_2$  and transient grating (TG) signals at  $\mathbf{k}_{TG} = -\mathbf{k}_1 + \mathbf{k}'_1 + \mathbf{k}_2$ . In Table 2, we summarize these FWM signals. In the case of overlapping pulses, the interaction operator eq 13 is no

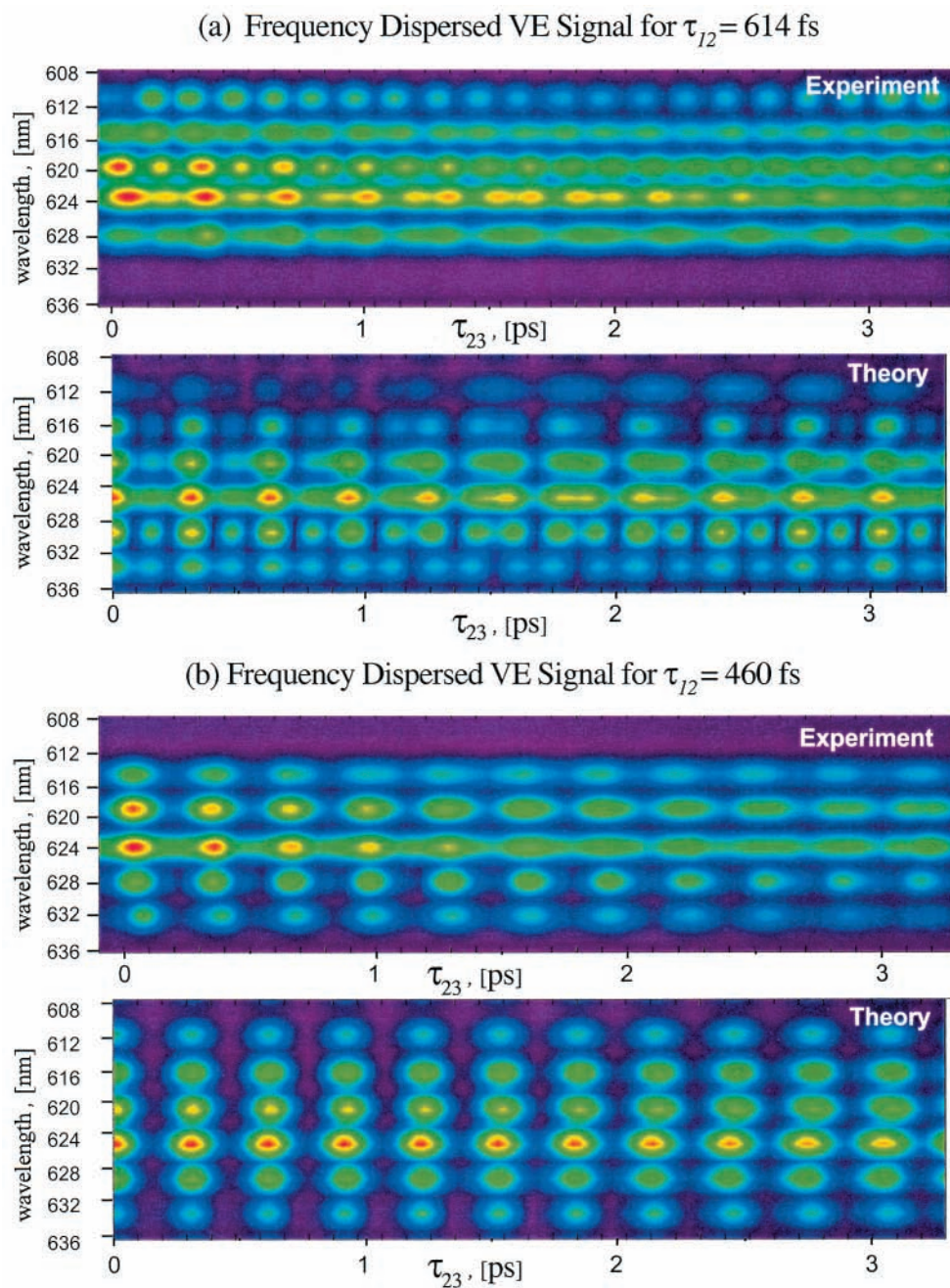


**Figure 5.** Experimental data and simulation of the VE frequency dispersed signal when (a)  $\tau_{12} = 460$  fs and (b)  $\tau_{12} = 614$  fs. The frequency dispersed signal shows the contribution of each polarization emitting with a central wavelength indicated on the vertical axis as a function of the time delay  $\tau_{23}$  of the scanning pulse. The lighter regions of the plot correspond to the higher intensity of the signal. In Figure 5a, we show the two-dimensional spectra when  $\tau_{12} = 614$  fs. The transient shows fast oscillations with a period that corresponds to the vibrational frequency of the ground state. There is a small contribution from a population in the excited state that is apparent in the 628 nm spectral region. In Figure 5b, we show the two-dimensional spectra corresponding to  $\tau_{12} = 460$  fs. The transient only shows oscillations with a period that corresponds to the vibrational frequency of the excited state.

longer proportional to the spectrum of the pulse. The reverse photon echo can be observed when the first two pulses overlap in time. This process (not included in Table 2) is observed in three electronic state systems.<sup>124,125</sup>

Experimental FWM signal obtained with three noncollinear pulses, when one pair of pulses overlaps in time, are displayed in Figure 6. The transients, along with their fast Fourier transform and the DSFD are shown for the X–B transition of  $I_2$ . The RTG signal is presented in Figure 6a as a function of the delay time  $\tau$  between the scanning pulse  $\mathbf{k}_1$  and the overlapped pulses  $\mathbf{k}_2$  and  $-\mathbf{k}'_2$ . Examining the DSFD, the signal depends on the time evolution of the vibronic coherence induced

by the first pulse. The RTG transient initially oscillates with the 307 fs excited-state period. This is because the contribution of the molecular response  $R_1$  (responsible for the excited-state dynamics) does not require specific values of the time delay between the first two interactions as does  $R_4$  that is maximized for  $\tau = 2\pi n/\omega_e$ . However, at a latter time, the excited-state anharmonicity and the inhomogeneous dephasing attenuates this contribution and the excited and ground-state components become comparable. The ground-state oscillation period of 160 fs is apparent for the transient for  $\tau > 3$  ps. The contribution of both dynamics is confirmed by the Fourier analysis showing a larger contribution at the excited-state vibrational frequency

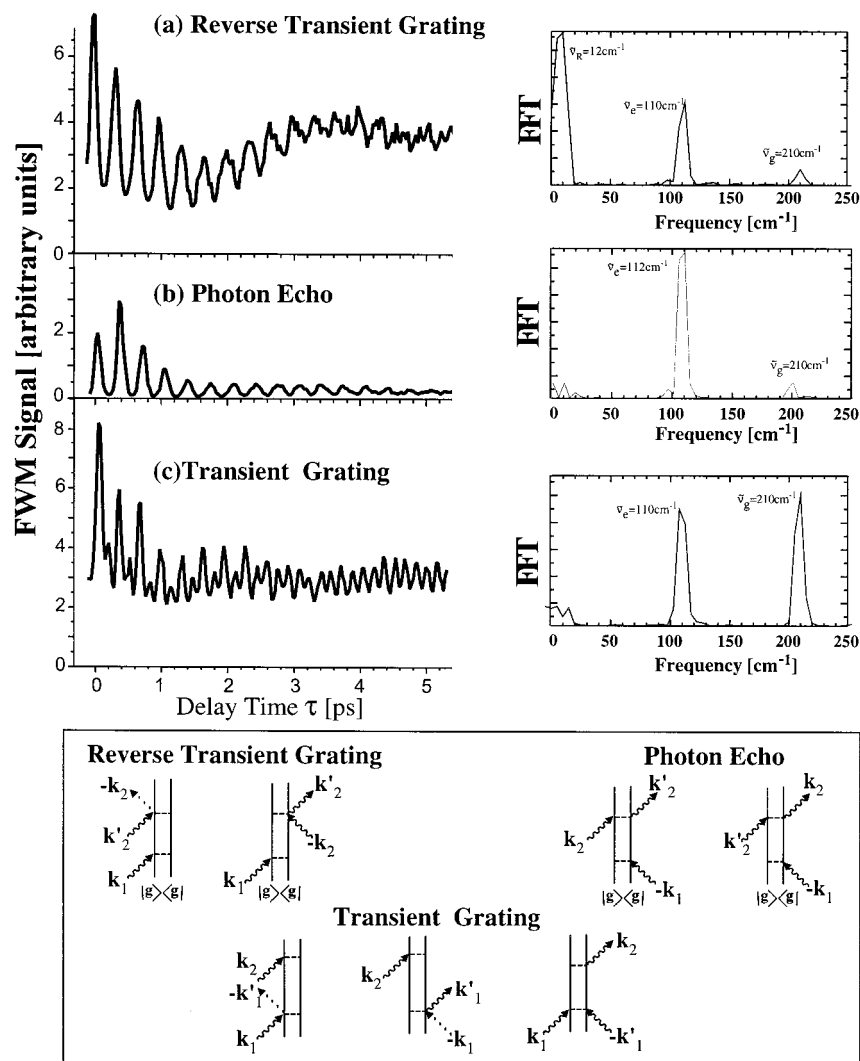


**Figure 6.** Experimental transients, their Fourier transform, and the corresponding DSFD for FWM processes having two pulses overlapped in time, for the B–X transition of  $\text{I}_2$ . The reverse transient grating signal is presented as a function of the delay time  $\tau$  (see Table 2). The RTG signal initially oscillates with the excited-state period ( $T_e = 307$  fs), and at a latter time,  $\tau > 3$  ps, the ground-state oscillation (with a period  $T_g = 160$  fs) is apparent. This is confirmed by the Fourier analysis showing contributions at the excited and ground-state vibrational frequencies. The low-frequency components in the FFT correspond to rotational motion. The DSFD indicates that the probing pulse interrogates excited-state populations, whereas the ground-state dynamics present in the transient can be attributed to the initial thermal distribution of the vibrational modes. The photon echo transient is obtained as a function of the delay time  $\tau$  (see Table 2). A direct comparison between the reverse-transient grating and photon echo transients reveals that the slow undulation (2 ps) in the RTG measurement, corresponding to the rotational dephasing, is absent in the PE transient. Transient grating data is obtained as a function of the delay time  $\tau$  (see Table 2). The TG signal shows ground- and excited-state oscillations. This result is in agreement with its respective DSFD.

compared with that at the ground-state frequency. The rotational contribution peaks at a frequency smaller than  $20 \text{ cm}^{-1}$ . Notice the slow modulation in the signal caused by the rotational motion characteristic of nonrephasing spectroscopic techniques. The PE signal is shown in Figure 6b. From the DSFD, we see that the signal depends on the time evolution of the vibronic coherence induced by the first pulse on the bra. The data corresponds to excited-state vibrational dynamics from contributions from both  $R_2$  and  $R_3$  molecular responses. Excited-state dynamics are probed in  $R_2$  as a function of time  $\tau_{13}$  and in  $R_3$  as a function of time  $\tau_{12}$ . In PE,  $\tau_{12} = \tau_{13} = \tau$ ; therefore, both  $R_2$  and  $R_3$  contribute to the signal with excited-state dynamics. This molecular response does not require specific values of the time delay between the first two interactions (as does the contribution of  $R_3$  responsible for the ground-state dynamics) and is therefore the prevalent contribution to the PE signal. A direct comparison the RTG and PE transients reveals that the rotational modulation and the background are smaller in the PE transient. This difference is also apparent in the FFT of the PE and the RTG

transients; the rotational contribution (peaks at frequencies  $< 20 \text{ cm}^{-1}$ ) in the photon echo FFT are greatly reduced. This is due to the cancellation of the rotational and vibrational phases, leading to the rephasing of the coherence, present in photon echo techniques. In a PE, the first field interaction is on the bra side of the diagram producing an initial coherence opposite in sign with respect to the third-order coherence (see Figure 3). Reversing the coherence leads to the rephasing of the signal.<sup>42</sup> This is in contrast to a RTG process, where the first field interaction is on the ket side producing a first-order coherence with the same sign as the third-order coherence. The experimental capability for distinguishing bra from ket interactions is clearly displayed in these transients (Figure 6 parts a and b) where the only experimental difference is the geometry of the laser pulses. TG data is included in Figure 6c. The transient and the Fourier analysis show ground- and excited-state dynamics along with a weak rotational modulation.

Overlapping three degenerate laser pulses in time leads to a strong signal that contains all of the Liouville path contributions

described above. The signal depends on the wavelength of the pulses only because the two time delays are set to zero. This arrangement, also known as degenerate four-wave mixing (DFWM), can be used in the frequency domain where enhanced spectral resolution results from the eighth-order dependence of the signal on the transition dipole moment.<sup>126</sup> DFWM can also be used as a probing mechanism in time-resolved experiments initiated by a pump pulse.<sup>50</sup>

## VII. Local Field Induced Signals

The description of nonlinear spectroscopic methods given so far assumes that all electric field interactions involve the external laser pulses. Additional nonlinear processes are possible that involve the participation of electric fields generated in the sample from polarized molecules. Each odd-order polarization emits an electromagnetic field that can yield a new nonlinear signal.<sup>127–130</sup> The participation of an electric field from an induced polarization in the system gives rise to new effects known as local field and cascading. They stem from the linear and the nonlinear polarization, respectively.<sup>13,127</sup> Processes involving a first-order polarization are observable when gas-phase samples with long-coherence lifetimes and interaction lengths interact with ultrafast pulses. This situation is best detected using pulse sequences for which ordinary FWM signals are forbidden.<sup>38,100,129,131,132</sup>

The interaction of ultrafast lasers with samples having long coherence times yields new nonlinear optical signals resulting from a local field effects.<sup>13</sup> This signal is attributable to a process in which one ensemble of molecules undergoes a first-order electric field interaction that induces an electronic coherence,  $P^{(1)}(t)$ . The field resulting from the first-order polarization, which may last for hundreds of picoseconds for a diluted sample,<sup>24</sup> interacts with a second molecular ensemble that has undergone two electric field interactions (or a population transfer). The FWM signal arises from the third-order polarization of the second molecular ensemble.<sup>13,100</sup> The local field FWM signal will be detected at the  $\mathbf{k}_{\parallel}$  phase-matching direction if the population transfer is initiated with a ket interaction and at the  $\mathbf{k}_{\perp}$  direction otherwise. This process can be clearly detected using pulse sequences that yield no signal in the rotating wave approximation.

The induced first-order electric field is given by

$$E_{\text{induced}}^{(1)}(\mathbf{r}, t) \propto P^{(1)}(\mathbf{r}, t) = \text{Tr}[\hat{\mu}\hat{\rho}^{(1)}(\mathbf{r}, t)] = \sum_{e,g} \mu_{eg} \exp[-\gamma_{eg}(t-t_1)] (V_{eg,1} \exp[-i\omega_{eg}(t-t_1)] + c.c.) \quad (48)$$

where the dependence with the spatial variable is implicit in the interaction operator,  $V_{eg,1}$ , see eqs 10–11. The local field induced third-order coherence can be derived from eq 8 when  $n = 3$ ,<sup>133</sup> replacing  $E_3(\mathbf{r}, t)$  by  $E_{\text{induced}}^{(1)}(\mathbf{r}, t)$

$$\rho_{egC}^{(3)}(\mathbf{r}, t) \propto \frac{2}{\hbar} i \exp[-(i\omega_{eg} + \gamma_{eg})(t-t_3)] \int_{-\infty}^t dt' \left( \sum_{g'} \mu_{eg'} \rho_{g'g}^{(2)}(\mathbf{r}, t_3) \exp[i\omega_{eg'}t'] - \sum_{e'} \mu_{e'g} \rho_{ee'}^{(2)}(\mathbf{r}, t_3) \exp[i\omega_{e'g}t'] \right) \sum_{e_1, g_1} \mu_{e_1 g_1} \exp[-\gamma_{e_1 g_1}(t' - t_1)] \times (V_{e_1 g_1, 1}^- \exp[-i\omega_{e_1 g_1}(t' - t_1)] + V_{e_1 g_1, 1}^+ \exp[i\omega_{e_1 g_1}(t' - t_1)]) \quad (49)$$

The expression for  $\hat{\rho}^{(2)}(\mathbf{r}, t)$  can be obtained from eq A2.

## Local Field Induced Three-Pulse FWM

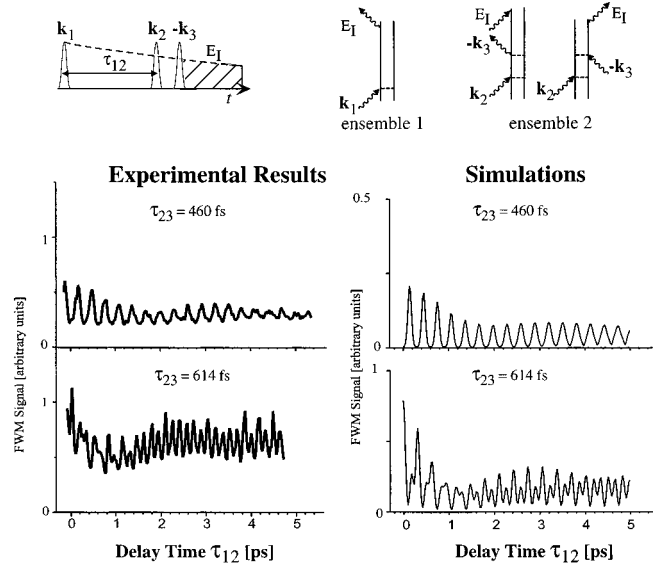


**Figure 7.** Experimental and calculated C-FID FWM signal along with its pulse sequence and the DSFD for the B-X transition of  $I_2$ . The time delay between the pulses that form the population,  $\tau_{23}$ , controls the observation of ground-state (oscillation period 160 fs) or excited-state (oscillation period 307 fs) vibrational motion. The ensemble 1 diagram induces the first-order electronic coherence emission,  $E_1$ , that cascaded into the ensemble 2 diagrams. Only the emission arising from the ensemble 2 diagrams contributes to the signal. Notice the similarity between these diagrams and the VE diagrams (see Table 1); in the cascaded experiment, the third field is replaced by the induced first-order polarization of the first ensemble.

$\hat{\rho}^{(2)}(\mathbf{r}, t)$  have both spatial components,  $(-\mathbf{k}_2 + \mathbf{k}_3) \cdot \mathbf{r}$  and  $(\mathbf{k}_3 - \mathbf{k}_2) \cdot \mathbf{r}$ . The main contribution to the signal arises from the resonant terms; therefore, the cascaded third-order coherence is reduced to

$$\rho_{egC}^{(3)}(\mathbf{r}, t) \propto \frac{2}{\hbar} i \exp[-(i\omega_{eg} + \gamma_{eg}) \times (t-t_3)] \left( \sum_{g'} \mu_{eg'}^2 \rho_{g'g}^{(2)}(\mathbf{r}, t_3) V_{eg',1} \exp[i\omega_{eg'}t_1] f_{eg'}(t-t_1) - \sum_{e'} \mu_{e'g}^2 \rho_{ee'}^{(2)}(\mathbf{r}, t_3) V_{e'g,1} \exp[i\omega_{e'g}t_1] f_{e'g}(t-t_1) \right) \quad (50)$$

where the function  $f_{eg}(t-t_1)$  is defined by

$$f_{eg}(t-t_1) = \int_{-\infty}^{t-t_1} dt' \exp[-\gamma_{eg}t' + i(\omega_{e'g'} - \omega_{eg})t'] |_{e'=e, g'=g} \quad (51)$$

The phase matching direction of the resulting emission is  $\mathbf{k}_1 = (-\mathbf{k}_2 + \mathbf{k}_3) + \mathbf{k}_{\text{LF}}$ . The modulation of the local field FWM signal is given by the ground or excited-state vibrational dynamics as indicated by the factors  $\rho_{g'g}^{(2)}(\mathbf{r}, t_3)$  and  $\rho_{ee'}^{(2)}(\mathbf{r}, t_3)$ , respectively. The observed dynamics can be controlled by the time delay between the pulses that produce the population.<sup>100</sup>

Local field induced three pulse FWM signals were detected in GaAs quantum wells<sup>132</sup> and in gas-phase molecular iodine using nonlinear pulses arranged in forward box geometry.<sup>100</sup> Ground- and excited-state dynamics were observed by fixing the time delay  $\tau_{23} = 2(n+1)\pi/(\omega_e)$  and  $\tau_{23} = 2(n+1)\pi/(\omega_g)$ , respectively. In Figure 7, we present the experimental data and simulation carried out with eq 50. The pulse sequence and the DSFD corresponding to the third-order cascaded process are also included. Note that in the pulse sequence of this experiment



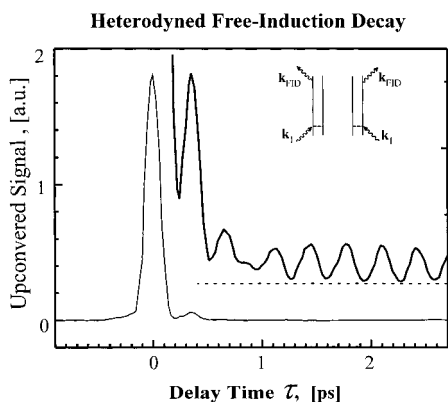


**Figure 8.** Experimental heterodyned free-induction decay data and the corresponding double sided Feynman diagrams (inset). The signal corresponds to the up-converted optical emission of the induced electric field by a femtosecond gate pulse in a nonlinear optical crystal. The scan (lower trace) includes the pump pulse centered at  $\tau = 0$ . The upper trace, resulting from the magnification of the data at 250 fs, shows modulations in the signal caused by the wave packet dynamics in the B state of iodine.

the scanning pulse is reversed in time with respect to the VE technique (see Table 1). Indeed, comparing Figure 4 with Figure 7, we see that both signals show similar dynamics except for the low intensity of the cascaded data. The similarity of the signals is emphasized when comparing the DSFD of the VE process (see Table 1) with the diagram of the second ensemble in Figure 7, in which the third pulse was replaced by the first-order induced electric field. The calculation of the cascaded data reproduces the vibrational structure of the experimental results.<sup>100</sup> Note that the data show femtosecond resolution even though the induced field decays with inhomogeneous decay  $T_2 \approx 200$  ps.<sup>24</sup> The induced electric field can maintain the femtosecond resolution of the experiment provided it is modulated on the femtosecond time scale. The first-order electric field emission is modulated and acts as a train of femtosecond laser pulses. The induced first-order electric field emission was measured (see Figure 8). The measurements of the heterodyned free induction decay signal (first-order electric field emission) were obtained with a femtosecond local oscillator pulse by up conversion in a second harmonic generation crystal.<sup>100</sup> The transient obtained along with its DSFD are shown in Figure 8.

Cascading FWM processes in strong field nonlinear experiments have been calculated<sup>134–139</sup> and observed.<sup>112,140–143</sup> These processes have been applied for the generation of new spectral components<sup>144–146</sup> and determination of the third-order nonlinear susceptibilities of noncentrosymmetric materials at several wavelengths.<sup>147–149</sup> In six-wave mixing experiments, there is a possibility that the FWM signal from the first three pulses cascades with the two additional pulses to create a cascaded FWM signal.

## VIII. Time-resolved Pump–Probe Spectroscopy

**A. Fluorescence Detected Pump–Probe.** The pump–probe technique can be considered as a heterodyned third order process resulting from the interaction with two pulses. In this technique, each of the pulses interacts twice with the sample producing populations and vibrational coherences. As long as the pump and the probe pulses are well separated temporally the signal depends on the population transferred and vibrational coherences by each pulse and not on electronic coherences, the wave function formalism can be used to describe these experiments.<sup>7–9</sup> Generally the pump–probe signal carries ground-state as well

as excited-state dynamics.<sup>14–16</sup> Pump–probe experiments can be carried out with different wavelengths to detect exclusively ground- or excited-state dynamics. In these cases, the pump–probe signal can be detected by monitoring the fluorescence or ion yield resulting from the probing step. These experiments involve three electronic states, and the signal is proportional to the transferred population into the final excited state.<sup>150,151</sup>

The success of the wave-function-based formalism for describing pump–probe experimental signals<sup>8,10,152</sup> can be attributed to the fact that the signal arises primarily from the vibrational population and vibrational coherence dynamics, arising from the double interaction of each pulse, and that relaxation processes are slow and do not involve an electronic coherence. For that reason, pump–probe experiments, in general, are not sensitive to the optical phase of the pump and the probe pulses in phase space. These experiments can also be interpreted using density-matrix wave packets resulting in the doorway/window formalism.<sup>20</sup> A pump creates a doorway wave packet that propagates during the delay time  $\tau$ ; the probe creates a window wave packet in the phase-space region monitored by the probe. The probe absorption spectrum is expressed as the overlap of the two wave packets. The main advantages of this representation are (1) it applies for both resonant and off-resonant experiments, (2) it allows the incorporation of solvation dynamics with arbitrary time scales (homogeneous and inhomogeneous line broadening), and (3) the result based on nonlinear response functions can be directly compared to other nonlinear spectroscopies.

In Figure 9, we show pump–probe signals of gas-phase iodine along with the DSFD contributing to the pump–probe spectrum in a three-level system. Pioneering experiments were carried out by the groups of Zewail<sup>18,71,153,154</sup> and Fleming.<sup>155,156</sup> In this experiment, a pump pulse at 620 nm excites the iodine molecules to the B state and the probing pulse at 310 nm excites the B population to the upper fluorescence state  $f_g$ . The signal was obtained as a function of the delay time  $\tau$  between the pulses with parallel (upper transient) or perpendicular (lower transient) relative polarization of the pump and the probe pulses. The transients contain oscillations with a period of 300 fs corresponding to the excited state vibrational frequency, whereas the amplitude is modulated by rotational dephasing. Because the intensity of the induced fluorescence is proportional to the population transferred into the B state, the technique can only monitor the motion on the first excited state as indicated by the DSFD 1 and 2 in Figure 9. Each molecular excitation (or photon absorption) is represented by two electric field interactions. After the pump, the molecular system is described by a population in the intermediate excited state,  $\rho_{ee}^{(2)}$ . The probe excites a fraction of the population in state  $|e\rangle$  to state  $|f\rangle$  again by a double electric field interaction. The pump–probe signal is proportional to the population in the intermediate excited state  $|e\rangle$ . The contribution of the third Liouville pathway (3) is negligible, and it is only comparable with the sequential contribution when both pulses overlap in time.<sup>14,20</sup>

**B. Direct Detection of Pump–Probe.** The absorption pump–probe signal field is detected along the direction of the probe,  $\mathbf{k}_2$ , and can be thought as an intrinsic heterodyne detection of a TG process, in which the heterodyned field is the probing electric field. The detected signal corresponds to the change in the energy of the transmitted probe pulse as a function of the time delay between the pump and the probe. This results in a linear detected signal (with respect to the induced polarization) that is preferable for quantification purposes. These experiments can be used to study energy relaxation<sup>157,158</sup> of both ground and

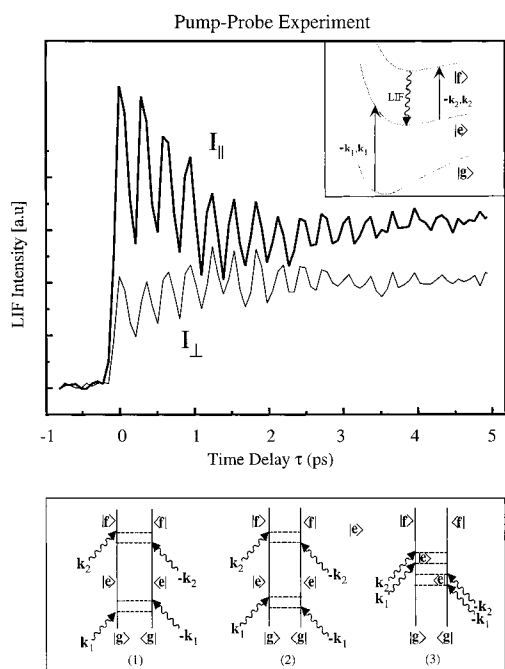


**Figure 9.** Experimental pump-probe transient obtained for  $I_2$  in the gas phase (data from ref 159) along with the DSFD contributing to the signal in a three-level system. In this experiment, a pump pulse at 620 nm excites the iodine molecules to the B state ( $|e\rangle$ ), and a probing pulse at 310 nm excites the B state population to the upper fluorescent ion-pair state  $f_g$  ( $|f\rangle$ ). The transient was obtained as a function of the delay time  $\tau$  between pulses with parallel (upper transient) and perpendicular (lower transient) relative polarization between the polarization vector of the lasers. The oscillations in the transient correspond to the excited-state vibrational period, whereas the amplitude is modulated by the rotational dephasing. In a sequential pump-probe experiment (as presented here), only the left two diagrams contribute to the detected signal.

excited states. Note that energy and population relaxation can be studied using some of the FWM techniques such as transient grating. Dephasing of electronic coherence cannot be measured by pump-probe methods.

**C. Phase-Locked Spontaneous Emission.** This method is an important variation on the pump-probe technique. The experiment involves a pair of pulses that are phase-locked. The signal corresponds to the spontaneous fluorescence detected at right angles that depends on both laser beams (selected by a lock-in amplifier). Scherer et al. used this technique on molecular iodine and showed the importance of phase locking to obtain the electronic coherence in the sample.<sup>27</sup> In these measurements, each femtosecond phase-locked pulse resonantly excites a vibronic coherence in the sample. The signal corresponds to the interference between the two electronic coherences. The destructive or constructive interference gives rise to an enhanced or diminished fluorescence, depending on the time delay between the pulses and their relative phase. From these measurements, it is possible to obtain the time dependent first-order polarization, or by the Fourier transform, it is possible to obtain the linear susceptibility near the locked frequency. These measurements are therefore closely related to photon echo measurements.<sup>13</sup> By combining the data from in-phase and quadrature fluorescence, it is possible to obtain the real (absorptive) and imaginary (dispersive) contributions of the optically induced linear material response.<sup>155</sup>

## IX. Conclusions

Over the past decade ultrafast molecular dynamics have been probed in real time using multiple-pulse techniques. The

observed signal can depend on population transfer to and from ground states and electronic coherence resulting from the nonlinear interaction between lasers and molecules and from vibrational and rotational coherences within a particular electronic state. The goal of this article is to discuss all possible signals that can be generated by ultrafast time-resolved experiments interacting resonantly with a molecular sample. Experimental results are presented for many of the ultrafast techniques discussed. These techniques can be classified according to the type of signal they measure. Population, vibrational and rotational coherences are measured with transient grating, virtual echo, CARS, CSRS, and pump-probe methods. Electronic coherences are measured with photon echo, stimulated photon echo, reverse transient grating, time-gated free-induction decay, and phase locked pump-probe methods. We have given the interpretation of signals from these techniques and their simulation based on the density matrix formalism and its diagrammatic representation. We have included formulas based on this formalism. For a simple model that can be used to simulate experimental data for a diatomic system such as molecular iodine. This model can be easily modified to simulate other systems with higher dimensionality. Here we summarize the main advantages of the density matrix approach.

The density matrix formulation incorporates the statistical nature of a molecular ensemble; therefore, this approach is most appropriate for describing coherent processes in inhomogeneous samples. Similarly it can easily incorporate all of the relevant intramolecular modes and their initial population of a polyatomic system from the outset. A wave function treatment would require the calculation to be repeated for each possible initial state. The straightforward incorporation of multiple modes and their relaxation parameters makes this formulation desirable for describing systems where collisional effects cannot be neglected.

(1) The density matrix formalism along with its diagrammatic representation allows tracking the transformation of the molecular sample resulting from the interaction with each pulse. For each successive interaction, populations and coherences are identified and their contribution to the measured nonlinear signal is quantified.

(2) The interpretation of each step of laser-matter interaction in a nonlinear experiment permits the selectivity of the electronic dynamics with a control parameter.

(3) The spatial dependence ( $\mathbf{k}_1 \cdot \mathbf{r}$  or  $\mathbf{k}_2 \cdot \mathbf{r}$ ) of FWM experiments with noncollinear beams allows the discrimination between different processes. The spatial dependence must be taken into account in any experiment that measures coherence involving the interaction of noncollinear pulses because it determines the phase matching condition.

(4) The explicit bookkeeping of the time evolution of the bra and the ket is an ideal approach to describe experiments sensitive to the sign of the electric field wave vector. This distinction is apparent when examining the PE and RTG transients, for example. The differentiation between bra and ket interactions arises in any measurement on the basis of the coherence resulting from the interaction between lasers and molecules.

(5) The density matrix takes into account the existence of different species in the sample, their individual dynamics, different relaxation processes, and the coherent couplings caused by the presence of each laser field. This allows the calculation of macroscopic and microscopic coherences that result from the interaction of a number of laser pulses with a system that is initially in a mixed state.

(6) The density matrix allows the direct calculation of the

frequency-dispersed signal, eqs 30 and 32, for different FWM processes as a function of spectroscopic parameters (Franck–Condon factors and the spectral intensity of the pulses) and the time delays between the pulses.

(7) The density matrix approach allows the calculation of cascaded FWM signals, eq 37.

**Acknowledgment.** The Dantus group gratefully acknowledges funding from the National Science Foundation (CHE-9812584) to carry out the experimental measurements and the support by the Chemical Sciences, Geosciences and Biosciences Division, Office of Basic Energy Sciences, Office of Science, U.S. Department of Energy for the analysis and theoretical work in our group. The work of the Mukamel group was supported by the National Science Foundation (CHE-0132571), the Chemical Sciences Division of the Office of Basic Energy Sciences of the U.S. Department of Energy and the National Institutes of Health (GM59230-01A2). This support is gratefully acknowledged. S.M. wishes to thank the Alexander von Humboldt Foundation for their generous support and hospitality while this work was carried out. M.D. is a Lucille and David Packard Science and Engineering Fellow, a Camille Dreyfus Teacher-Scholar, and an Alfred P. Sloan Fellow. B.I.G. thanks professor Mukamel and his colleagues for their hospitality during her stay at the University of Rochester. We thank I. Pastirk for his efforts to collect all of the data presented in this article and for his help to collect all of the references. The authors thank the reviewers for their suggestions.

## Appendix A. Expressions for Density Matrix Elements

Let us express the matrix elements of order  $n$  in terms of  $\hat{\rho}^{(0)}$ . In the case of a single-short pulse excitation, we have

$$\rho_{ab}^{(1)}(\mathbf{r}, t) = \frac{i}{\hbar} I_{ab}(t - t_1) V_{ab,1} (\rho_{bb}^{(0)} - \rho_{aa}^{(0)}) \quad (\text{A1})$$

This equation describes a first order ket or bra interaction depending if  $\omega_{ab}$  is positive or negative, see eq 8. Then, the operator  $I_{ab}(t - t_1)$  propagates the ket or the bra, respectively. Note that only the matrix elements with indices  $a$  and  $b$  that satisfy the RWA are nonzero.

A second-order interaction leads to  $\rho_{ab}^{(2)}(\mathbf{r}, t)$

$$\rho_{ab}^{(2)}(\mathbf{r}, t) = \left( \frac{i}{\hbar} \right)^2 I_{ab}(t - t_2) \sum_{c=1} \left\{ V_{ca,2} I_{cb}(t_2 - t_1) V_{cb,1} (\rho_{bb}^{(0)} - \rho_{cc}^{(0)}) + V_{cb,2} I_{ca}(t_2 - t_1) V_{ca,1} (\rho_{aa}^{(0)} - \rho_{cc}^{(0)}) \right\} \quad (\text{A2})$$

elements, given by  $(\mathbf{k}_1 - \mathbf{k}_2) \cdot \mathbf{r}$ ,  $(-\mathbf{k}_1 + \mathbf{k}_2) \cdot \mathbf{r}$ ,  $(-\mathbf{k}_1 - \mathbf{k}_2) \cdot \mathbf{r}$ , and  $(\mathbf{k}_1 + \mathbf{k}_2) \cdot \mathbf{r}$ . If the system consists of two electronic state coupled by a dipole transition, these spatial components reduce to  $(\mathbf{k}_1 - \mathbf{k}_2) \cdot \mathbf{r}$  and  $(-\mathbf{k}_1 + \mathbf{k}_2) \cdot \mathbf{r}$ , see Figure 2. In this particular case, the spatial components can be separated if eq A2 is rearranged in the following way:

$$\rho_{ab}^{(2)}(\mathbf{r}, t) = \left( \frac{i}{\hbar} \right)^2 I_{ab}(t - t_2) \sum_{c=1} \left\{ V_{ca,2}^- I_{cb}(t_2 - t_1) V_{cb,1}^+ (\rho_{bb}^{(0)} - \rho_{cc}^{(0)}) + V_{cb,2}^+ I_{ca}(t_2 - t_1) V_{ca,1}^- (\rho_{aa}^{(0)} - \rho_{cc}^{(0)}) \right\} \quad (\text{A3})$$

The spatial components  $(\mathbf{k}_1 - \mathbf{k}_2) \cdot \mathbf{r}$  and  $(-\mathbf{k}_1 + \mathbf{k}_2) \cdot \mathbf{r}$  are given by the products  $V_{ca,2}^- V_{cb,1}^+$  and  $V_{ca,2}^+ V_{cb,1}^-$ , respectively. Note that

$\rho_{ab}^{(2)}(\mathbf{r}, t)$  is nonzero if the indices  $a$  and  $b$  belong to levels of the same electronic state because of the RWA.

A third-order interaction leads to  $\rho_{ab}^{(3)}(\mathbf{r}, t)$

$$\rho_{ab}^{(3)}(\mathbf{r}, t) = \left( \frac{i}{\hbar} \right)^3 I_{ab}(t - t_3) \left\{ \begin{aligned} & \sum_{d=1} V_{ad,3} I_{db}(t_3 - t_2) \sum_{c=1} V_{cd,2} I_{cb}(t_2 - t_1) V_{cb,1} \rho_{bb}^{(0)} + \\ & \sum_{d=1} V_{db,3} I_{ad}(t_3 - t_2) \sum_{c=1} V_{dc,2} I_{ac}(t_2 - t_1) V_{ac,1} \rho_{cc}^{(0)} + \\ & \sum_{d=1} V_{ad,3} I_{db}(t_3 - t_2) \sum_{c=1} V_{cb,2} I_{cd}(t_2 - t_1) V_{cd,1} \rho_{dd}^{(0)} + \\ & \sum_{d=1} V_{db,3} I_{bd}(t_3 - t_2) \sum_{c=1} V_{ac,2} I_{dc}(t_2 - t_1) V_{dc,1} \rho_{cc}^{(0)} \end{aligned} \right\} \quad (\text{A4})$$

For a system of two electronic states coupled with a dipole interaction, this equation can be recast as follows:

$$\rho_{ab}^{(3)}(\mathbf{r}, t) = \left( \frac{i}{\hbar} \right)^3 I_{ab}(t - t_3) \left\{ \begin{aligned} & \sum_{d=1} V_{ad,3}^+ I_{db}(t_3 - t_2) \sum_{c=1} V_{cd,2}^- I_{cb}(t_2 - t_1) V_{cb,1}^+ \rho_{bb}^{(0)} + \\ & \sum_{d=1} V_{db,3}^+ I_{ad}(t_3 - t_2) \sum_{c=1} V_{dc,2}^- I_{ac}(t_2 - t_1) V_{ac,1}^+ \rho_{cc}^{(0)} + \\ & \sum_{d=1} V_{ad,3}^+ I_{db}(t_3 - t_2) \sum_{c=1} V_{cb,2}^+ I_{cd}(t_2 - t_1) V_{cd,1}^- \rho_{dd}^{(0)} + \\ & \sum_{d=1} V_{db,3}^+ I_{bd}(t_3 - t_2) \sum_{c=1} V_{ac,2}^+ I_{dc}(t_2 - t_1) V_{dc,1}^- \rho_{cc}^{(0)} \end{aligned} \right\} \quad (\text{A5})$$

Two spatial components are apparent in this expression, given by the products of the dipole interaction matrix elements. One component has a spatial dependence  $\mathbf{k}_1 \cdot \mathbf{r} = (\mathbf{k}_3 - \mathbf{k}_2 + \mathbf{k}_1) \cdot \mathbf{r}$ , from terms with products  $V_{ij,3}^+ V_{ij,2}^- V_{ij,1}^+$ , and the other has a spatial dependence  $\mathbf{k}_1 \cdot \mathbf{r} = (\mathbf{k}_3 + \mathbf{k}_2 - \mathbf{k}_1) \cdot \mathbf{r}$ , from terms with  $V_{ij,3}^+ V_{ij,2}^+ V_{ij,1}^-$ . Note that  $\rho_{ab}^{(3)}(t)$  is nonzero if the indices  $a$  and  $b$  belong to different electronic states because of the RWA.

## Appendix B. Expressions for Interference Terms

### 1. Four Level System, Dipole Coupling Interaction.

$$S_{\text{int},I}(\tau_{12}, \tau_{23}) = S_{R_2;R_2,I}(\tau_{12}, \tau_{23}) + S_{R_2;R_3,I}(\tau_{12}, \tau_{23}) + S_{R_3;R_2,I}(\tau_{12}, \tau_{23}) + S_{R_3;R_3,I}(\tau_{12}, \tau_{23}) \quad (\text{B1})$$

where

$$S_{R_3;R_3,I}(\tau_{12}, \tau_{23}) = \frac{\gamma}{4} \exp[-2\gamma\tau_{13}] \cos^2\left(\frac{\omega_e\tau_{12}}{2}\right) \left[ \cos^2\left(\frac{\omega_g\tau_{13}}{2}\right) + w^2 \sin\left(\frac{\omega_g\tau_{13}}{2}\right) \left[ \frac{4}{\gamma^2 + \omega_g^2} - \cos(\omega_g\tau_{23}) \left( \frac{2}{\gamma^2 + \omega_g^2} + \frac{1}{\gamma^2 + (\omega_e - \omega_g)^2} + \frac{1}{\gamma^2 + (\omega_e + \omega_g)^2} \right) \right] \right] \quad (\text{B2})$$

$$S_{R_2;R_3I}(\tau_{12},\tau_{23}) + S_{R_2;R_3I}(\tau_{12},\tau_{23}) = \frac{\gamma}{2} \exp[-2\gamma\tau_{13}] \cos\left(\frac{\omega_e\tau_{13}}{2}\right) \cos\left(\frac{\omega_e\tau_{12}}{2}\right) \left[ \cos\left(\frac{\omega_g\tau_{13}}{2}\right) \cos\left(\frac{\omega_g\tau_{12}}{2}\right) + w^2 \sin\left(\frac{\omega_g\tau_{13}}{2}\right) \sin\left(\frac{\omega_g\tau_{12}}{2}\right) \right] \left[ \cos\left(\frac{(\omega_e + \omega_g)\tau_{23}}{2}\right) \times \left( \frac{1}{\gamma^2 + \omega_e^2} - \frac{1}{\gamma^2 + \omega_g^2} - \frac{1}{\gamma^2 + (\omega_g + \omega_e)^2} \right) + \cos\left(\frac{(\omega_g - \omega_e)\tau_{23}}{2}\right) \left( \frac{1}{\gamma^2 + \omega_e^2} - \frac{1}{\gamma^2 + \omega_g^2} - \frac{1}{\gamma^2 + (\omega_g - \omega_e)^2} \right) \right] \quad (\text{B3})$$

$$S_{R_2;R_2I}(\tau_{12},\tau_{23}) = \frac{\gamma}{4} \exp[-2\gamma\tau_{13}] \cos^2\left(\frac{\omega_e\tau_{13}}{2}\right) \times \left[ \cos^2\left(\frac{\omega_g\tau_{12}}{2}\right) + w^2 \sin^2\left(\frac{\omega_g\tau_{12}}{2}\right) \right] \left[ \frac{-4}{\gamma^2 + \omega_g^2} + \cos(\omega_g\tau_{23}) \times \left( \frac{2}{\gamma^2 + \omega_e^2} - \frac{1}{\gamma^2 + (\omega_e - \omega_g)^2} - \frac{1}{\gamma^2 + (\omega_e + \omega_g)^2} \right) \right] \quad (\text{B4})$$

Note that the term  $S_{R_3;R_3I}$  ( $S_{R_2;R_2I}$ ) is canceled when the time delay  $\tau_{12}$  ( $\tau_{13}$ ) is  $\tau_{12} = 2\pi(n + 0.5)/\omega_e$  [ $\tau_{13} = 2\pi(n + 0.5)/\omega_e$ ]. These delay times lead to the suppression of  $S_I$  ground-state dynamics. The term  $S_{R_3;R_3I} + S_{R_3;R_2I}$  is canceled when  $\tau_{12} = 2\pi(n + 0.5)/\omega_e$  and  $\tau_{13} = 2\pi(n + 0.5)/\omega_e$  corresponding to the observation of the excited-state vibrational dynamics. However, when the  $S_I$  signal oscillates mainly with ground-state vibrational period, for delay times  $\tau_{12} = 2\pi(n + 0.5)/\omega_g$  and  $\tau_{13} = 2\pi(n + 0.5)/\omega_g$ , the interference term is not canceled. The interference term contribution contains a linear combination of excited and ground-state periods. In gas phase  $\omega_e, \omega_g \gg \gamma$ , and the interference contribution to the signal is very small, leading to an effective selection of the vibrational dynamics.

Interference terms for the  $S_{II}$  signal of a four level system

$$S_{\text{int},II}(\tau_{12},\tau_{23}) = S_{R_1;R_1II}(\tau_{12},\tau_{23}) + S_{R_1;R_4II}(\tau_{12},\tau_{23}) + S_{R_4;R_1II}(\tau_{12},\tau_{23}) + S_{R_4;R_4II}(\tau_{12},\tau_{23}) \quad (\text{B5})$$

where

$$S_{R_4;R_4II}(\tau_{12},\tau_{23}) = \frac{\gamma}{4} \exp[-2\gamma\tau_{13}] \cos^2\left(\frac{\omega_g\tau_{23}}{2}\right) \cos^2\left(\frac{\omega_e\tau_{12}}{2}\right) \left[ \frac{4(1 + w^2)}{\gamma^2 + \omega_e^2} - \cos(\omega_g\tau_{13})(1 - w^2) \left( \frac{2}{\gamma^2 + \omega_g^2} + \frac{2}{\gamma^2 + (\omega_e - \omega_g)^2} \right) \right] \quad (\text{B6})$$

$$S_{R_1;R_4II}(\tau_{12},\tau_{23}) + S_{R_4;R_1II}(\tau_{12},\tau_{23}) = \frac{\gamma}{2} \exp[-2\gamma\tau_{13}] \cos\left(\frac{\omega_g\tau_{23}}{2}\right) \cos\left(\frac{\omega_e\tau_{12}}{2}\right) \left\{ \left[ -\frac{1}{\gamma^2 + \omega_e^2} + \frac{1}{\gamma^2 + \omega_g^2} + \frac{1}{\gamma^2 + (\omega_g + \omega_e)^2} \right] \cos\left(\frac{(\omega_g + \omega_e)\tau_{13}}{2}\right) \cos\left(\frac{\omega_g\tau_{12}}{2}\right) - w^2 \sin\left(\frac{(\omega_g + \omega_e)\tau_{13}}{2}\right) \sin\left(\frac{\omega_g\tau_{12}}{2}\right) \right\} + \left[ -\frac{1}{\gamma^2 + \omega_e^2} + \frac{1}{\gamma^2 + \omega_g^2} + \frac{1}{\gamma^2 + (\omega_g - \omega_e)^2} \right] \left[ \cos\left(\frac{(\omega_g - \omega_e)\tau_{13}}{2}\right) \cos\left(\frac{\omega_g\tau_{12}}{2}\right) - w^2 \sin\left(\frac{(\omega_g - \omega_e)\tau_{13}}{2}\right) \sin\left(\frac{\omega_g\tau_{12}}{2}\right) \right] \quad (\text{B7})$$

$$S_{R_1;R_1II}(\tau_{12},\tau_{23}) = \frac{\gamma}{4} \exp[-2\gamma\tau_{13}] \cos^2\left(\frac{\omega_e\tau_{23}}{2}\right) \left[ \cos^2\left(\frac{\omega_g\tau_{12}}{2}\right) + w^2 \sin^2\left(\frac{\omega_g\tau_{12}}{2}\right) \right] \left[ \frac{4}{\gamma^2 + \omega_g^2} + \cos(\omega_e\tau_{13}) \times \left( \frac{2}{\gamma^2 + \omega_e^2} - \frac{1}{\gamma^2 + (\omega_e - \omega_g)^2} - \frac{1}{\gamma^2 + (\omega_e + \omega_g)^2} \right) \right] \quad (\text{B8})$$

For the experimental conditions that lead to excited state observation,  $\tau_{12} = 2\pi(n + 0.5)/\omega_e$ , the interference term is not suppressed and contributes with excited-state dynamics,  $S_{R_1;R_1II}$ , to the  $S_{II}$  signal. However, for experimental conditions in which the excited-state dynamics is suppressed,  $\tau_{23} = 2\pi(n + 0.5)/\omega_e$ , the contribution of the interference term contains a linear combination of the ground- and excited-state vibrational periods. In any case, the contribution of this term is negligible in gas-phase systems.

## References and Notes

- (1) *Ultrafast Phenomena XII*; Elsaesser, T., Mukamel, S., Murnane, M. M., Scherer, N. F., Eds.; Springer-Verlag: Berlin, 2000.
- (2) Zewail, A. H. *Femtochemistry: ultrafast dynamics of the chemical bond*; World Scientific: Singapore, 1994; Vols. I and II.
- (3) Manz, J.; Wöste, L. *Femtosecond Chemistry*; VCH: Weinheim, Germany, 1995; Vols. I and II.
- (4) Chergui, M. *Femtochemistry: Ultrafast Chemical and Physical Processes in Molecular Systems*; World Scientific: Singapore, 1996.
- (5) Special Issue dedicated to Femtochemistry. *J. Chem. Phys.* **1998**, *102*.
- (6) De Schryver, F. C.; Feyter, S. D.; Schweitzer, G. *Femtochemistry*; Wiley-VCH: Weinheim, Germany, 2001.
- (7) Tannor, D. J.; Rice, S. A. *J. Chem. Phys.* **1985**, *83*, 5013.
- (8) Williams, S. O.; Imre, D. G. *J. Phys. Chem.* **1988**, *92*, 6648.
- (9) Metiu, H.; Engel, V. *J. Opt. Soc. Am. B* **1990**, *7*, 1709.
- (10) Gruebele, M.; Zewail, A. H. *J. Chem. Phys.* **1993**, *98*, 883.
- (11) Shen, Y. R. *The Principle of Nonlinear Optics*; Wiley: New York, 1984.
- (12) Boyd, R. W. *Nonlinear Optics*; Academic Press: San Diego, CA, 1992.
- (13) Mukamel, S. *Principles of Nonlinear Optical Spectroscopy*; Oxford University Press: New York, 1995.
- (14) Yan, Y. J.; Fried, L. E.; Mukamel, S. *J. Phys. Chem.* **1989**, *93*, 8149.
- (15) Fried, L. E.; Mukamel, S. *J. Chem. Phys.* **1990**, *93*, 3063.
- (16) Mukamel, S. *Annu. Rev. Phys. Chem.* **1990**, *41*, 647.
- (17) Dantus, M.; Rosker, M. J.; Zewail, A. H. *J. Chem. Phys.* **1987**, *87*, 2395.
- (18) Dantus, M.; Rosker, M. J.; Zewail, A. H. *J. Chem. Phys.* **1988**, *89*, 6128.

- (19) Pastirk, I.; Brown, E. J.; Grimberg, B. I.; Lozovoy, V. V.; Dantus, M. *Faraday Discuss.* **1999**, *113*, 401.
- (20) Yan, Y. J.; Mukamel, S. *Phys. Rev. A* **1990**, *41*, 6485.
- (21) Yan, Y. J.; Mukamel, S. *J. Chem. Phys.* **1991**, *94*, 179.
- (22) Mukamel, S. *Annu. Rev. Phys. Chem.* **2000**, *51*, 691.
- (23) Mukamel, S.; Piryatinski, A.; Chernyak, V. *Acc. Chem. Res.* **1999**, *32*, 145.
- (24) Pastirk, I.; Lozovoy, V. V.; Dantus, M. *Chem. Phys. Lett.* **2001**, *333*, 76.
- (25) Tannor, D. J.; Kosloff, R.; Rice, S. A. *J. Chem. Phys.* **1986**, *85*, 5805.
- (26) Neuhauser, D.; Rabitz, H. *Acc. Chem. Res.* **1993**, *26*, 496.
- (27) Scherer, N. F.; Ruggiero, A. J.; Du, M.; Fleming, G. R. *J. Chem. Phys.* **1990**, *93*, 856.
- (28) Zhu, L. C.; Kleiman, V.; Li, X. N.; Lu, S. P.; Trentelman, K.; Gordon, R. J. *Science* **1995**, *270*, 77.
- (29) Assion, A.; Baumert, T.; Bergt, M.; Brixner, T.; Kiefer, B.; Seyfried, V.; Strehle, M.; Gerber, G. *Science* **1998**, *282*, 919.
- (30) Levis, R. J.; Menkir, G. M.; Rabitz, H. *Science* **2001**, *292*, 709.
- (31) Sim, E.; Makri, N. *J. Chem. Phys.* **1995**, *102*, 5616.
- (32) Makri, N. *Annu. Rev. Phys. Chem.* **1999**, *50*, 167.
- (33) Wang, H. B.; Thoss, M.; Müller, W. H. *J. Chem. Phys.* **2000**, *112*, 47.
- (34) Yan, Y. J.; Mukamel, S. *J. Chem. Phys.* **1988**, *89*, 5160.
- (35) Sepulveda, M. A.; Mukamel, S. *J. Chem. Phys.* **1995**, *102*, 9327.
- (36) Ovchinnikov, M.; Apkarian, V. A.; Voth, G. A. *J. Chem. Phys.* **2001**, *114*, 7130.
- (37) Heller, E. J. *Acc. Chem. Res.* **1981**, *14*, 368.
- (38) Ovchinnikov, M.; Apkarian, V. A. *J. Chem. Phys.* **1997**, *106*, 5775.
- (39) Cina, J. A. *J. Chem. Phys.* **2000**, *113*, 9488.
- (40) Donoso, A.; Martens, C. C. *Phys. Rev. A* submitted for publication.
- (41) Stock, G.; Domcke, W. *Phys. Rev. A* **1992**, *45*, 3032.
- (42) Patel, C. K. N.; Slusher, R. E. *Phys. Rev. Lett.* **1968**, *20*, 1087.
- (43) Heritage, J. P.; Gustafson, T. K.; Lin, C. H. *Phys. Rev. Lett.* **1975**, *34*, 1299.
- (44) Fayer, M. D. *Annu. Rev. Phys. Chem.* **1982**, *33*, 63.
- (45) Rose, T. S.; Fayer, M. D. *Chem. Phys. Lett.* **1985**, *117*, 12.
- (46) Rose, T. S.; Wilson, W. L.; Wäckerle, G.; Fayer, M. D. *J. Chem. Phys.* **1987**, *86*, 5370.
- (47) Morgen, M.; Price, W.; Hunziker, L.; Ludowise, P.; Blackwell, M.; Chen, Y. *Chem. Phys. Lett.* **1993**, *209*, 1.
- (48) Morgen, M.; Price, W.; Ludowise, P.; Chen, Y. *J. Chem. Phys.* **1995**, *102*, 8780.
- (49) Hayden, C. C.; Chandler, D. W. *J. Chem. Phys.* **1995**, *103*, 10465.
- (50) Motzkus, M.; Pedersen, S.; Zewail, A. H. *J. Phys. Chem.* **1996**, *100*, 5620.
- (51) Schmitt, M.; Knopp, G.; Materny, A.; Kiefer, W. *Chem. Phys. Lett.* **1997**, *270*, 9.
- (52) Schmitt, M.; Knopp, G.; Materny, A.; Kiefer, W. *Chem. Phys. Lett.* **1997**, *280*, 339.
- (53) Meyer, S.; Schmitt, M.; Materny, A.; Kiefer, W.; Engel, V. *Chem. Phys. Lett.* **1997**, *281*, 332.
- (54) Chen, T.; Engel, V.; Heid, M.; Kiefer, W.; Knopp, G.; Materny, A.; Meyer, S.; Pausch, R.; Schmitt, M.; Schwoerer, H.; Siebert, T. *J. Mol. Struct.* **1999**, *481*, 33.
- (55) Meyer, S.; Schmitt, M.; Materny, A.; Kiefer, W.; Engel, V. *Chem. Phys. Lett.* **1998**, *287*, 753.
- (56) Frey, H. M.; Beaud, P.; Gerber, T.; Mischler, B.; Radi, P. P.; Tzannis, A. P. *Appl. Phys. B* **1999**, *68*, 735.
- (57) Knopp, G.; Pinkas, I.; Prior, Y. *J. Raman Spectrosc.* **2000**, *31*, 51.
- (58) Brown, E. J.; Zhang, Q.; Dantus, M. *J. Chem. Phys.* **1999**, *110*, 5772.
- (59) Pastirk, I.; Lozovoy, V. V.; Grimberg, B. I.; Brown, E. J.; Dantus, M. *J. Phys. Chem. A* **1999**, *103*, 10226.
- (60) Brown, E. J.; Pastirk, I.; Grimberg, B. I.; Lozovoy, V. V.; Dantus, M. *J. Chem. Phys.* **1999**, *111*, 3779.
- (61) Lozovoy, V. V.; Grimberg, B. I.; Brown, E. J.; Pastirk, I.; Dantus, M. *J. Raman Spectrosc.* **2000**, *31*, 41.
- (62) Pinkas, I.; Knopp, G.; Prior, Y. *J. Chem. Phys.* **2001**, *115*, 236.
- (63) Dantus, M. *Annu. Rev. Phys. Chem.* **2001**, *52*, 639.
- (64) Rubner, O.; Schmitt, M.; Knopp, G.; Materny, A.; Kiefer, W.; Engel, V. *J. Phys. Chem. A* **1998**, *102*, 9734.
- (65) Lang, T.; Motzkus, M.; Frey, H. M.; Beaud, P. *J. Chem. Phys.* **2001**, *115*, 5418.
- (66) Hertz, E.; Chaux, R.; Faucher, O.; Lavorel, B. *J. Chem. Phys.* **2001**, *115*, 3598.
- (67) Pastirk, I.; Comstock, M.; Dantus, M. *Chem. Phys. Lett.* **2001**, *349*, 71.
- (68) Mulliken, R. S. *J. Chem. Phys.* **1971**, *55*, 288.
- (69) Tellinghuisen, J. *J. Quant. Spectrosc. Radiat. Transfer* **1978**, *19*, 149.
- (70) Bowman, R. M.; Dantus, M.; Zewail, A. H. *Chem. Phys. Lett.* **1989**, *161*, 297.
- (71) Dantus, M.; Bowman, R. M.; Zewail, A. H. *Nature* **1990**, *343*, 737.
- (72) Lozovoy, V. V.; Titov, A. A.; Gostev, F. E.; Tovbin, D. G.; Antipin, S. A.; Umanskii, S. Y.; Sarkisov, O. M. *Chem. Phys. Reports* **1998**, *17*, 1267.
- (73) Lozovoy, V. V.; Pastirk, I.; Brown, E. J.; Grimberg, B. I.; Dantus, M. *Int. Rev. Phys. Chem.* **2000**, *19*, 531.
- (74) Neumann, J. V. *Mathematical Foundations of Quantum Mechanics*; Princeton University Press: Princeton, NJ, 1955.
- (75) Blum, K. *Density Matrix Theory and Applications*; Plenum Press: New York, 1996.
- (76) Zwanzig, R. *Lect. Theo. Phys.* **1961**, *3*, 106.
- (77) Mukamel, S. *Phys. Reports* **1982**, *93*, 1.
- (78) Fano, U. *Phys. Rev.* **1963**, *131*, 259.
- (79) Sakurai, J. J. *Modern Quantum Physics*; Addison-Wesley Publ. Co.: New York, 1994; Vol. I.
- (80) Lee, D.; Albrecht, A. C. In *Advances in Infrared and Raman Spectroscopy*; Clark, R. J. H., Hester, R. E., Eds.; Wiley-Heyden: Chichester, U.K., 1985; Vol. 12.
- (81) Mukamel, S.; Ciordas-Ciurdariu, C.; Khidekel, V. *IEEE J. Quantum Electron.* **1996**, *32*, 1278.
- (82) Mukamel, S.; Ciordas-Ciurdariu, C.; Khidekel, V. *Adv. Chem. Phys.* **1997**, *101*, 345.
- (83) Mukamel, S. *J. Chem. Phys.* **1997**, *107*, 4165.
- (84) Meier, T.; Chernyak, V.; Mukamel, S. *J. Chem. Phys.* **1997**, *107*, 8759.
- (85) Tanimura, Y.; Mukamel, S. *J. Chem. Phys.* **1993**, *99*, 9496.
- (86) Mukamel, S.; Piryatinski, A.; Chernyak, V. *J. Chem. Phys.* **1999**, *110*, 1711.
- (87) Scheurer, C.; Piryatinski, A.; Mukamel, S. *J. Am. Chem. Soc.* **1996**, *118*, 3114.
- (88) Siebert, T.; Schmitt, M.; Michelis, T.; Materny, A.; Kiefer, W. *J. Raman Spectrosc.* **1999**, *30*, 807.
- (89) Lozovoy, V. V.; Grimberg, B. I.; Pastirk, I.; Dantus, M. *Chem. Phys.* **2001**, *267*, 99; Special Issue on Laser Control of Quantum Dynamics.
- (90) Yokojima, S.; Meier, T.; Chernyak, V.; Mukamel, S. *Phys. Rev. B* **1999**, *59*, 12584.
- (91) Zadoyan, R.; Kohen, D.; Lidar, D. A.; Apkarian, V. A. *Chem. Phys.* **2001**, *266*, 323.
- (92) Zadoyan, R.; Apkarian, V. A. *Chem. Phys. Lett.* **2000**, *326*, 1.
- (93) Cho, M.; Rosenthal, S. J.; Scherer, N. F.; Ziegler, L. D.; Fleming, G. R. *J. Chem. Phys.* **1992**, *96*, 5033.
- (94) Bigot, J. Y.; Mycek, M. A.; Weiss, S.; Ulbrich, R. G.; Chemla, D. S. *Phys. Rev. Lett.* **1993**, *70*, 3307.
- (95) de Boeij, W. P.; Pshenichnikov, M. S.; Wiersma, D. A. *Chem. Phys. Lett.* **1995**, *238*, 1.
- (96) Lepetit, L.; Cheriaux, G.; Joffre, M. *J. Opt. Soc. Am. B* **1995**, *12*, 2647.
- (97) Lepetit, L.; Joffre, M. *Opt. Lett.* **1996**, *21*, 564.
- (98) Hahn, E. L. *Phys. Rev.* **1950**, *80*, 580.
- (99) Ernst, R. R.; Bodenhausen, G.; Wokaum, A. *Principles of nuclear magnetic resonance in one and two dimensions*; Oxford University Press: New York, 1987; Vol. 14.
- (100) Lozovoy, V. V.; Pastirk, I.; Comstock, M.; Dantus, M. *Chem. Phys.* **2001**, *266*, 205.
- (101) Yang, T.-S.; Zhang, R.; Myers, A. *J. Chem. Phys.* **1994**, *100*, 8573.
- (102) Siebert, T.; Schmitt, M.; Vierheilg, A.; Flachenecker, G.; Engel, V.; Materny, A.; Kiefer, W. *J. Raman Spectrosc.* **2000**, *31*, 25.
- (103) Pausch, R.; Heid, M.; Chen, T.; Kiefer, W.; Schwoerer, H. *J. Chem. Phys.* **1999**, *110*, 9560.
- (104) Schmitt, M.; Knopp, G.; Materny, A.; Kiefer, W. *J. Phys. Chem. A* **1998**, *102*, 4059.
- (105) Schoenlein, R. W.; Mittleman, D. M.; Shiang, J. J.; Alivisatos, A. P.; Shank, C. V. *Phys. Rev. Lett.* **1993**, *70*, 1014.
- (106) Bardeen, C. J.; Shank, C. V. *Chem. Phys. Lett.* **1993**, *203*, 535.
- (107) Cho, M.; Yu, J.-Y.; Taiha, J.; Nagasawa, Y.; Passino, S. A.; Fleming, G. R. *J. Phys. Chem.* **1996**, *100*, 11944.
- (108) de Boeij, W. P.; Pshenichnikov, M. S.; Wiersma, D. A. *Chem. Phys. Lett.* **1996**, *253*, 53.
- (109) de Boeij, W. P.; Pshenichnikov, M. S.; Wiersma, D. A. *Annu. Rev. Phys. Chem.* **1998**, *49*, 99.
- (110) Pshenichnikov, M. S.; de Boeij, W. P.; Wiersma, D. A. *Phys. Rev. Lett.* **1996**, *76*, 4701.
- (111) Chachisvilis, M.; Fidler, H.; Sundström, V. *Chem. Phys. Lett.* **1995**, *234*, 141.
- (112) Kirkwood, J. C.; Albrecht, A. C. *J. Raman Spec.* **2000**, *31*, 107.
- (113) Materny, A.; Chen, T.; Schmitt, M.; Siebert, T.; Vierheilg, A.; Engel, V.; Kiefer, W. *Appl. Phys. B* **2000**, *71*, 299.
- (114) Gerstenkorn, S.; Luc, P. *J. Phys. (Paris)* **1985**, *46*, 867.
- (115) Vohringer, P.; Arnett, D. C.; Yang, T. S.; Scherer, N. F. *Chem. Phys. Lett.* **1995**, *237*, 387.
- (116) Hybl, J. D.; Albrecht, A. W.; Faeder, S. M. G.; Jonas, D. M. *Chem. Phys. Lett.* **1998**, *297*, 307.
- (117) Yakovlev, V.; Bardeen, C. J.; Che, J.; Cao, J.; Wilson, K. R. *J. Chem. Phys.* **1998**, *108*, 2309.

- (118) Lozovoy, V. V.; Antipin, S. A.; Gostev, F. E.; Titov, A. A.; Tovbin, D. G.; Sarkisov, O. M.; Vetchinkin, A. S.; Umanskii, S. Y. *Chem. Phys. Lett.* **1998**, *284*, 221.
- (119) Hornung, T.; Meier, R.; Motzkus, M. *Chem. Phys. Lett.* **2000**, *326*, 445.
- (120) Rabitz, H.; de Vivie-Riedle, R.; Motzkus, M.; Kompa, K. *Science* **2000**, *288*, 824.
- (121) Hornung, T.; Motzkus, M.; de Vivie-Riedle, R. *J. Chem. Phys.* **2001**, *115*, 3105.
- (122) Hornung, T.; Meier, R.; Zeidler, D.; Kompa, K. L.; Proch, D.; Motzkus, M. *Appl. Phys. B—Lasers Opt.* **2000**, *71*, 277.
- (123) Zeidler, D.; Frey, S.; Kompa, K. L.; Motzkus, M. *Phys. Rev. A* **2001**, *6402*, 3420.
- (124) Zhang, W. M.; Chernyak, V.; Mukamel, S. *J. Chem. Phys.* **1999**, *110*, 5011.
- (125) Leegwater, J. A.; Mukamel, S. *J. Chem. Phys.* **1994**, *101*, 7388.
- (126) Vaccaro, P. H. In *Molecular Dynamics and Spectroscopy by Stimulated Emission Pumping*; Dai, H. L., Field, R. W., Eds.; World Scientific: Singapore, 1995.
- (127) Mukamel, S.; Deng, Z.; Grad, J. *J. Opt. Soc. Am. B* **1988**, *5*, 804.
- (128) Mukamel, S. *Molecular Nonlinear Optics*; Academic Press: New York, 1994.
- (129) Leegwater, J. A.; Mukamel, S. *Phys. Rev. A* **1992**, *46*, 452.
- (130) Dubovsky, O.; Mukamel, S. *J. Chem. Phys.* **1991**, *95*, 7828.
- (131) Tortschanoff, A.; Muakmel, S. to be published.
- (132) Mukamel, S.; Leo, K.; Shah, J.; Chemla, D. S. *Phys. Rev. A* **1991**, *44*, 2124.
- (133) equation A5.
- (134) Wu, S. *J. Appl. Phys.* **1993**, 8035.
- (135) Unsbo, P. *J. Opt. Soc. Am. B* **1995**, *12*, 43.
- (136) Knoester, J.; Mukamel, S. *J. Opt. Soc. Am. B* **1988**, *6*, 643.
- (137) Knoester, J.; Mukamel, S. *Phys. Rev. A* **1989**, *39*, 1899.
- (138) Knoester, J.; Mukamel, S. *Phys. Rev. A* **1990**, *41*, 3812.
- (139) Spano, F. C.; Mukamel, S. *Phys. Rev. Lett.* **1991**, *66*, 1197.
- (140) Eifthimiopoulos, T.; Movsessian, M. E.; Katharakis, M.; Merlemis, N. *J. Appl. Phys.* **1996**, *80*, 639.
- (141) Blank, D. A.; Kaufman, L. J.; Fleming, G. R. *J. Chem. Phys.* **1999**, *111*, 3105.
- (142) Cho, M. H.; Blank, D. A.; Sung, J.; Park, K.; Hahn, S.; Fleming, G. R. *J. Chem. Phys.* **2000**, *112*, 2082.
- (143) Astinov, V.; Kubarych, K. J.; Milne, C. J.; Miller, R. J. D. *Chem. Phys. Lett.* **2000**, *327*, 334.
- (144) Lu, Z. W.; Wang, Q.; He, W. M.; Ma, Z. G. *Appl. Phys. B—Lasers Opt.* **1996**, *63*, 43.
- (145) Varanavicius, A.; Dubietis, A.; Berzanskis, A.; Danielius, R.; Piskarskas, A. *Opt. Lett.* **1997**, *22*, 1603.
- (146) Crespo, H.; Mendonca, J. T.; Dos Santos, A. *Opt. Lett.* **2000**, *25*, 829.
- (147) Zgonik, M.; Gunter, P. *J. Opt. Soc. Am. B* **1996**, *13*, 570.
- (148) Biaggio, I. *Phys. Rev. Lett.* **1999**, *82*, 193.
- (149) Bosshard, C.; Gubler, U.; Kaatz, P.; Mazerant, W.; Meier, U. *Phys. Rev. B* **2000**, *61*, 10688.
- (150) Dantus, M.; Rosker, M. J.; Zewail, A. H. *J. Chem. Phys.* **1988**, *89*, 6128.
- (151) Rosker, M. J.; Dantus, M.; Zewail, A. H. *J. Chem. Phys.* **1988**, *89*, 6113.
- (152) Cao, J.; Wilson, K. R. *J. Chem. Phys.* **1997**, *106*, 5062.
- (153) Rose, T. S.; Rosker, M. J.; Zewail, A. H. *J. Chem. Phys.* **1988**, *88*, 6672.
- (154) Khundkar, L. R.; Zewail, A. H. *Annu. Rev. Phys. Chem.* **1990**, *41*, 15.
- (155) Scherer, N. F.; Carlson, R. J.; Matro, A.; Du, M.; Ruggiero, A. J.; Romerorochin, V.; Cina, J. A.; Fleming, G. R.; Rice, S. A. *J. Chem. Phys.* **1991**, *95*, 1487.
- (156) Cho, M.; Scherer, N. F.; Fleming, G. R.; Mukamel, S. *J. Chem. Phys.* **1992**, *96*, 5618.
- (157) Nelson, K. A.; Ippen, E. P. *Adv. Chem. Phys.* **1989**, *75*, 1.
- (158) Fragnito, H. L.; Bigot, J.-Y.; Becker, P. C.; Shank, C. V. *Chem. Phys. Lett.* **1989**, *160*, 101.
- (159) Brown, E. J.; Pastirk, I.; Dantus, M. *J. Phys. Chem. A* **1999**, *103*, 2912.